Electromagnetic Oscillation Origin Location in Multiple-Inverter-Based Power Systems Using Components Impedance Frequency Responses

WEIHUA ZHOU[1], (Student Member, IEEE), RAYMUNDO E. TORRES-OLGUIN[2], MEHDI KARBALAYE ZADEH[3], (Member, IEEE), BEHROOZ BAHRANI[4], (Senior Member, IEEE), YANBO WANG[1], (Senior Member, IEEE), and ZHE CHEN[1], (Fellow, IEEE)

[1]Department of Energy Technology, Aalborg University, 9220 Aalborg, Denmark (e-mail: wez@et.aau.dk; ywa@et.aau.dk; zch@et.aau.dk)
[2]SINTEF Energy Research Institute, 7034 Trondheim, Norway (e-mail: raymundo.torres-olguin@sintef.no)
[3]Department of Marine Technology, Norwegian University of Science and Technology, 7491 Trondheim, Norway (e-mail: mehdi.zadeh@ntnu.no)
[4]Department of Electrical and Computer Systems Engineering, Monash University, 3800 Clayton VIC, Australia (e-mail:behrooz.bahrani@monash.edu)

Corresponding author: Zhe Chen (e-mail: zch@et.aau.dk).

ABSTRACT Existing impedance-based stability criterion (IBSC) for electromagnetic stability assessment of multiple-grid-connected-inverter (GCI)-based power systems suffers from several limitations. First, global stability feature is hard to be obtained if Nyquist-criterion-based IBSC is used. Second, heavy computational burdens caused by either right-half-plane (RHP) poles calculation of impedance ratios or nodal admittance matrix construction can be involved. Third, it's not easy to locate the oscillation origin, since the dynamics of individual components are missing in the aggregated load and source sub-modules. This article aims to overcome the aforementioned three limitations of the existing IBSC. First, frequency responses of the load impedance and source admittance defined at each node in a selected components aggregation path are obtained by aggregating individual components (e.g., GCIs and transmission lines), from which imaginary parts of RHP poles of these load impedances and source admittances are directly identified without knowing analytical expressions of these load impedances and source admittances. Then, based on the Nyquist plots of minor loop gains (defined as the ratios of the impedance frequency responses of these load and source sub-modules), stability features of these selected nodes are obtained. Finally, if some nodes are unstable, the oscillation origin is located based on numbers of the RHP poles of these load impedances and source admittances. Compared to the existing IBSC, the presented method can assess global stability and locate oscillation origin more efficiently. The local circulating current issue, as a main obstacle of the existing IBSC, can also be identified. Time-domain simulation results in Matlab/Simulink platform and real-time verification results in OPAL-RT platform of a four-GCI-based radial power plant validate the effectiveness of the presented electromagnetic oscillation origin location method.

INDEX TERMS Circulating current, impedance frequency responses, grid-connected inverter, impedance-based stability criterion, oscillation origin location.

Nomenclature

Abbreviations

AIM	Analytical impedance model.
GCI	Grid-connected inverter.
IBSC	Impedance-based stability criterion.
IFRs	Impedance frequency responses.
LIM	Loop impedance model.
MLG	Minor loop gain.
NAM	Nodal admittance model.
NC	Nyquist criterion.
P.u.l.	Per-uint-length.
PCC	Point of common coupling.
PLL	Phase-locked loop.
RHP	Right-half-plane.
TL	Transmission line.

This article has been accepted for publication in a future issue of this journal, but has not been fully edited. Content may change prior to final publication. Citation information: DOI 10.1109/OJIES.2020.3045620, IEEE Open Journal of the Industrial Electronics Society

Zhou *et al.*: Electromagnetic Oscillation Origin Location

VF, MF	Vector fitting and matrix fitting algorithms.

Symbols

ω_1	Grid fundamental angular frequency.
C_f	Filter capacitance.
f_{sw}, f_s, T_s	Switching frequency, sampling frequency, and sampling time.
I_g, I_g^*	Grid current and its reference.
$I_{g,d}^{ref}, I_{g,q}^{ref}$	The d-axis and q-axis grid current references.
I_K, I_K^*	Output current of GCI #K and its reference.
K_{cp}	Capacitor-current-feedback coefficient.
K_{ppll}, K_{ipll}	Proportional and integral gains of the PLL regulator.
K_p, K_i	Proportional and integral gains of the current regulator.
L_{f1}, L_{f2}	Inverter-side and grid-side filter inductances.
$S_{N_K}^{left}, I_{N_K}^{left}, Y_{N_K}^{left}$	Norton equivalent circuit of the left part of node N_K.
$S_{PCC}^{left}, I_{PCC}^{left}, Y_{PCC}^{left}$	Norton equivalent circuit of the left part of PCC.
$S_{N_K}^{right}, V_{N_K}^{right}, Z_{N_K}^{right}$	Thevenin equivalent circuit of the right part of node N_K.
$S_{PCC}^{right}, V_{PCC}^{right}, Z_{PCC}^{right}$	Thevenin equivalent circuit of the right part of PCC.
V_{dc}	DC-link voltage.
$Y_{N_K'}^{frrl}, Z_{N_K'}^{frrr}$	The admittance and impedance frequency responses by seeing leftward and rightward at the right side of node N_K'.
$Y_{N_K'}^{rl}, Z_{N_K'}^{rr}, Y_{N_K'}^{frrl}, Z_{N_K'}^{frrr}$	The admittance and impedance models by seeing leftward and rightward at the right side of node N_K', and their frequency resposnes.
$I_{N_K}^{GCI}, Y_{N_K}^{GCI}$	Current source and admittance of the Norton equivalent circuit of GCI #K.
$S_{N_j'}^{bot}, I_{N_j'}^{bot}, Y_{N_j'}^{bot}$	Norton equivalent circuit of the bottom part of node N_j'.
$S_{N_j'}^{left}, I_{N_j'}^{left}, Y_{N_j'}^{left}$	Norton equivalent circuit of the left part of node N_j'.
$S_{N_j'}^{lr}, V_{N_j'}^{lr}, Z_{N_j'}^{lr}$	Thevenin equivalent circuit by seeing rightward at the left side of node N_j'.
$S_{N_j'}^{right}, V_{N_j'}^{right}, Z_{N_j'}^{right}$	Thevenin equivalent circuit of the right part of node N_j'.
$S_{N_j'}^{rl}, I_{N_j'}^{rl}, Y_{N_j'}^{rl}$	Norton equivalent circuit by seeing leftward at the right side of node N_j'.
$T_{N_K}^{clm1}, T_{N_K}^{m1}$	Closed and open MLGs between $S_{N_K}^{left}$ and $S_{N_K}^{right}$ at node N_K.
$T_{PCC}^{clm1}, T_{PCC}^{m1}$	Closed and open MLGs between S_{PCC}^{left} and S_{PCC}^{right} at PCC.
$T_{N_q'}^{clml}, T_{N_q'}^{clmr}$	Closed MLGs between $S_{N_q'}^{right}$ and $S_{N_q'}^{bot}$, and between Z_{2q-2} and $S_{N_q'}^{rl}$ at node N_q'.
$T_{N_K'}^{clmrl}$	Closed MLG between $S_{N_K'}^{right}$ and $S_{N_K'}^{left}$ at node N_K'.
$T_{N_K'}^{clm}, T_{N_K'}^{m}$	Closed and open MLGs between $S_{N_K'}^{rl}$ and $S_{N_K'}^{right}$ at node N_K'.
$T_{N_p}^{clm}$	Closed MLG between Z_{2p-1} and GCI #p at node N_p.

I. INTRODUCTION

Recently, renewable energies, such as wind power and solar power, have been increasingly penetrating into the existing utility grid [1]. Voltage source grid-connected inverters (GCIs), as efficient power electronic interfaces, are widely used to transmit the generated electricity into the utility grid [2]. However, impedance interactions between various control loops of the GCIs (e.g., outer power control loop, dc-link voltage control loop, inner current control loop, and phase-locked loop (PLL)) and passive components (e.g., transmission lines (TLs), underground cables, and transformers) may cause electromagnetic oscillation phenomena in various frequency ranges [3]–[6]. Though oscillation mechanisms of single-GCI-based power plants have been thoroughly explored in [4], [7]–[11], the oscillation mechanism and oscillation origin location of multiple-GCI-based power plants need to be further investigated.

Impedance-based stability criterion (IBSC) was originally proposed in [12] to assess the stability of DC power systems, and then modified in [13], [14] to cope with AC power systems. The whole power plant is partitioned into load and source sub-modules at an arbitrary node, based on which impedance ratio of the load and source sub-modules is calculated. Both encirclement number of Nyquist plot of the impedance ratio around $(-1, j0)$ and number of right-half-plane (RHP) poles of the impedance ratio should be calculated [14], [15]. For single-GCI-based power plants, RHP poles calculation can be avoided, since both the GCI and the grid should be inherently stable [10], [14]. Furthermore, if the system is assessed as unstable, the oscillation origin can be located as the impedance interaction between the GCI and the grid. However, avoidance of RHP poles calculation and location of oscillation origin commonly cannot be achieved in multiple-GCI-based power plants by performing the Nyquist criterion (NC) one time at a selected node, since RHP poles may emerge during the components aggregation procedure, and the oscillation origin may be lost in the aggregated load and source sub-modules [16]–[18].

The RHP poles of the aggregated load and source sub-modules can be analytically derived based on system topology and impedance transfer functions of individual components [16], [17], [19]. However, this analytical approach

sometimes cannot be implemented in practice, since internal structures and parameters of the GCIs can be confidential due to industry secrecy. In addition, the orders of the load and source sub-modules may be very high if a huge number of GCIs exist in the power plant, which will result in heavy computational burdens. The vector fitting (VF) and matrix fitting (MF) algorithms initially proposed in [20], [21] can fit a set of discrete frequency responses by continuous transfer function and transfer matrix, respectively, which have been employed in [18], [22]–[25] to facilitate the stability assessment of power electronic-dominated power systems. Specifically, the VF algorithm is used in [18], [23] to fit discrete load impedance and source admittance frequency responses as continuous transfer functions, so that extraction of the RHP poles from the analytically-derived transfer functions can be avoided. Discrete loop impedance models (LIMs) are established in [26]–[28] by further aggregating the impedance frequency responses of the load and source sub-modules, based on which the MF algorithm is used to generate continuous LIMs, and zeros of the determinant of the fitted LIMs are identified. Although the RHP poles identification can be more efficient or even avoided with the help of the VF and MF algorithms, oscillation origin still cannot be located.

According to [17], [29], nodal admittance model (NAM) and the aforementioned LIM are dual pairs. Therefore, the zeros of the determinants of system NAMs are calculated in [30]–[32] for stability analysis. Similar to the LIM method, the RHP poles calculation can also be avoided in the NAM method. In addition, a frequency-domain component connection method is presented in [16], [33]–[35], where the generalized NC is applied on the return ratio of the impedance matrices of the connection network and the composite model of all inverters. Since the two impedance matrices can commonly be guaranteed to not have RHP poles, the RHP poles calculation in the generalized NC can be avoided. According to the discussions in [16], [35], the derived NAMs in [30]–[32] are exactly the closed-loop transfer function matrices of multiple-input-multiple-output negative feedback systems with feed-forward gain being 1 and feed-back gain being the return-ratio matrices derived in [16], [33]–[35]. Since admittance information of each GCI is stored in the derived NAM and return-ratio matrix, global stability feature can be obtained, and oscillation origin can further be located based on participation factor analysis [35]. However, orders of both the NAM and the return-ratio matrix can be high, which may lead to heavy computational burdens. In addition, once GCIs are added/removed into/from the power plant or system topology changes, the high-order NAM and return-ratio matrix should be re-calculated.

The NC and generalized NC are sequentially implemented from the farthest node to point of common coupling (PCC) of radial power plants in [36], [37] and [19], [38], [39], respectively. No RHP poles calculation is needed, since both load and source sub-modules are inherently stable in each step. In addition, the node where the (generalized) NC is not satisfied

is identified as the oscillation origin. Compared with the LIM, NAM, and component connection method, the multiple-step stability analysis method is more flexible, and can reduce the computational burdens. However, only stability of grid current instead of output currents of individual GCIs can be assessed, i.e., this analysis method cannot obtain global stability feature. Furthermore, the presented conditions in [19], [36]–[39] to guarantee the stability of grid current are sufficient yet not necessary.

To fill in the research gaps mentioned in the above literature review, a computationally efficient global stability analysis and oscillation origin location method based on only terminal impedance frequency responses of individual components is presented in this article. First, terminal impedance frequency responses of individual components are aggregated at both sides of each node in a selected components aggregation path. On its basis, RHP poles of these load and source sub-modules are directly identified from their impedance and admittance frequency responses, respectively. The stability of these selected nodes is then obtained with further help of the Nyquist plots of the impedance ratios. If a specific node is unstable, the oscillation origin is located based on numbers of RHP poles of these load and source sub-modules. Main contributions of this article can be highlighted as follows.

1) An NC-based sufficient and necessary condition for global stability is derived, where relation between global stability and local stability is discussed.

2) Based on the derived NC-based global stability condition, an efficient oscillation origin location method is presented. The problematic nodes where RHP poles occur during components aggregation can be identified.

3) RHP poles of load and source sub-modules for the NC are directly identified from load impedances and source admittances frequency responses, respectively, without knowing analytical expressions of load and source sub-modules, which can reduce the computational burdens and cope with black-box models.

4) Circulating current phenomenon is identified based on numbers of RHP poles of the load and source sub-modules along the selected components aggregation path.

5) A grid current stability enhancement method is initiated, i.e., the paralleled stable branch of an unstable branch is enforced to be the same as the unstable branch, which may be achieved by adjusting the transmission line impedance of the stable branch.

The rest of this article is organized as follows. In Section II, an NC-based sufficient and necessary condition for global stability of a representative radial power plant is derived. On its basis, the principle and implementation procedure of the presented global stability analysis and oscillation origin location method are explained in Section III. In Section IV, the presented method is implemented in a four-GCI-based radial power plant. The correctness of the theoretical analysis results in Section IV is validated in Section V. In Section VI, comparisons between the presented method and
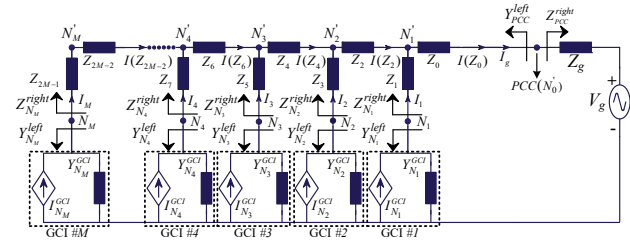
FIGURE 1. Equivalent circuit model of a representative radial grid-connected power plant [40].

FIGURE 2. IBSC at different nodes of Fig. 1. (a) At PCC. (b) At node N_K ($K \in [1, M]$).

existing IBSCs are performed. Finally, Section VII draws the conclusion.

II. AN NC-BASED SUFFICIENT AND NECESSARY CONDITION FOR GLOBAL STABILITY

Fig. 1 shows the single-line diagram of a radial grid-connected power plant, which consists of M GCIs. The detailed control structure of these GCIs are explained in Appendix A. If grid current I_g and output currents of all GCIs (i.e., I_1–I_M) are stable, the system is globally stable. The global stability can be assessed by further simplifying the equivalent circuit model in Fig. 1. The aggregation rules of two components/sub-modules during the circuit simplification procedure are stated here [18]. Each component/sub-module can be defined as either Y type or Z type which should be modeled as an Norton or a Thevenin equivalent circuit, respectively. In detail, individual GCIs and grid are defined as Y type and Z type, respectively. The transmission lines and underground cables are defined as Y type in parallel case and Z type in series case. Based on the definitions of individual components, the type of the aggregated sub-module of two components/sub-modules are further defined as follows. The aggregated sub-module is Z type, if two Z-type components/sub-modules are connected in parallel or in series, or one Z-type component/sub-module and one Y-type component/sub-module are connected in parallel. Furthermore, the aggregated sub-module is Y type, if two Y-type components/sub-modules are connected in parallel, or one Z-type component/sub-module and one Y-type component/sub-module are connected in series.

Based on the components/sub-modules aggregation rules, Fig. 1 can be simplified as Fig. 2(a) by representing the left and right parts of PCC as an Norton and a Thevenin equivalent circuit, respectively. In addition, Fig. 1 can be simplified as Fig. 2(b) by representing the left and right parts of node N_K ($K \in [1, M]$) as an Norton and a Thevenin equivalent circuit, respectively. Based on Fig. 2, I_g and I_K can be calculated as

$$I_g = \frac{I_{PCC}^{left} - V_{PCC}^{right} Y_{PCC}^{left}}{1 + Z_{PCC}^{right} Y_{PCC}^{left}} = T_{PCC}^{clm1} I_g^* \tag{1}$$

and

$$I_K = \frac{I_{N_K}^{left} - V_{N_K}^{right} Y_{N_K}^{left}}{1 + Z_{N_K}^{right} Y_{N_K}^{left}} = T_{N_K}^{clm1} I_K^* \tag{2}$$
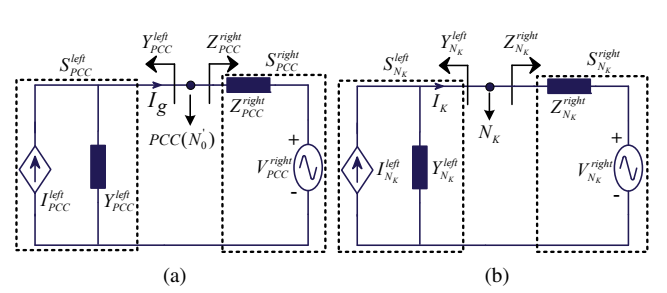
, respectively, where $T_{PCC}^{clm1} = (1 + Z_{PCC}^{right} Y_{PCC}^{left})^{-1}$, $I_g^* = I_{PCC}^{left} - V_{PCC}^{right} Y_{PCC}^{left}$, $T_{N_K}^{clm1} = (1 + Z_{N_K}^{right} Y_{N_K}^{left})^{-1}$, and $I_K^* = I_{N_K}^{left} - V_{N_K}^{right} Y_{N_K}^{left}$. Based on Appendix B, numbers of RHP poles of I_g and I_K can be calculated as

$$P(I_g) = P(T_{PCC}^{clm1}) = P(T_{PCC}^{m1}) + N_{(-1,j0)}(T_{PCC}^{m1}) \tag{3}$$

and

$$P(I_K) = P(T_{N_K}^{clm1}) = P(T_{N_K}^{m1}) + N_{(-1,j0)}(T_{N_K}^{m1}) \tag{4}$$

, respectively, where $P(\bullet)$ and $Z(\bullet)$ indicate number of RHP poles and RHP zeros, respectively. $N_{(-1,j0)}(\bullet)$ indicates encirclement number of Nyquist plot around $(-1, j0)$ in clockwise direction. In addition, $T_{PCC}^{m1} = Z_{PCC}^{right} Y_{PCC}^{left}$ and $T_{N_K}^{m1} = Z_{N_K}^{right} Y_{N_K}^{left}$. Since grid and GCI #$K$ ($K \in [1, M]$) are assumed to be inherently stable, Z_{PCC}^{right} and $Y_{N_K}^{left}$ do not have RHP poles [14]. However, Y_{PCC}^{left} and $Z_{N_K}^{right}$ may have RHP poles (This issue will be discussed in Section III-A.) [15].

A sufficient and necessary condition for the global stability of Fig. 1 can be summarized as follows.

Lemma 1: The radial grid-connected power plant in Fig. 1 is globally stable if and only if

1) I_g is stable, i.e., $P(T_{PCC}^{m1}) + N_{(-1,j0)}(T_{PCC}^{m1}) = 0$; and
2) I_K ($K \in [1, M]$) is stable, i.e., $P(T_{N_K}^{m1}) + N_{(-1,j0)}(T_{N_K}^{m1}) = 0$.

III. PRESENTED GLOBAL STABILITY ANALYSIS AND OSCILLATION ORIGIN LOCATION METHOD

In this section, the NC-based sufficient and necessary condition for global stability derived in Section II is reformulated. On its basis, the principle of the presented global stability analysis and oscillation origin location method is explained.

A. REFORMULATION OF THE NC-BASED SUFFICIENT AND NECESSARY CONDITION FOR GLOBAL STABILITY

Based on the components/sub-modules aggregation rules in Section II, the components aggregation procedure of Fig. 1 from left to right is shown in Fig. 3(a), which consists of three main steps at each node. Take node N_K' ($K \in [1, M]$) as an example. In step 1, Z_{2K-1} and GCI #K are aggregated as $S_{N_K'}^{bot}$. In step 2, $S_{N_K'}^{left}$ at the left of node N_K' and $S_{N_K'}^{bot}$ at the bottom of node N_K' are further aggregated as $S_{N_K'}^{rl}$ (The
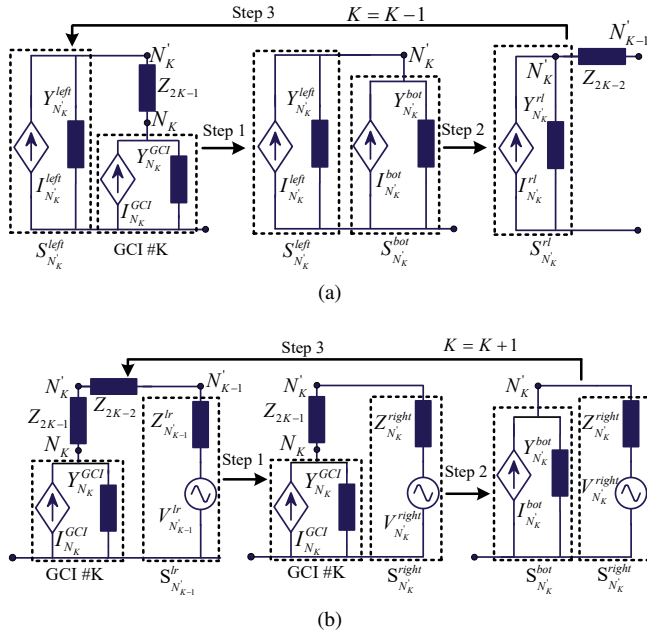
(a)

(b)

FIGURE 3. Components aggregation procedures at node N'_K in Fig. 1. (a) From left to right. (b) From right to left.

superscript rl means that $S^{rl}_{N'_K}$ is the aggregated sub-module by seeing leftward at the right side of node N'_K. In step 3, $S^{rl}_{N'_K}$ and Z_{2K-2} are aggregated as $S^{left}_{N'_{K-1}}$. The parameters of $S^{bot}_{N'_K}$, $S^{rl}_{N'_K}$, and $S^{left}_{N'_{K-1}}$ are calculated as

$$I^{bot}_{N'_K} = T^{clm}_{N_K} I^{GCI}_{N_K} \qquad Y^{bot}_{N'_K} = T^{clm}_{N_K} Y^{GCI}_{N_K} \qquad (5)$$

$$I^{rl}_{N'_K} = I^{left}_{N'_K} + I^{bot}_{N'_K} \qquad Y^{rl}_{N'_K} = Y^{left}_{N'_K} + Y^{bot}_{N'_K} \qquad (6)$$

and

$$I^{left}_{N'_{K-1}} = T^{clmr}_{N'_K} I^{rl}_{N'_K} \qquad Y^{left}_{N'_{K-1}} = T^{clmr}_{N'_K} Y^{rl}_{N'_K} \qquad (7)$$

, respectively, where $T^{clm}_{N_K} = (1 + Z_{2K-1} Y^{GCI}_{N_K})^{-1}$ and $T^{clmr}_{N'_K} = (1 + Z_{2K-2} Y^{rl}_{N'_K})^{-1}$. The Norton equivalent circuit of the left part of node N'_K ($K \in [0, M]$) in Fig. 1 can then be derived based on Fig. 3(a) and (5)-(7) using recursive method, shown as

$$I^{left}_{N'_K} = \sum_{p=K+1}^{M} (T^{clm}_{N_p} I^{GCI}_{N_p} \prod_{q=K+1}^{p} T^{clmr}_{N'_q})$$

$$Y^{left}_{N'_K} = \sum_{p=K+1}^{M} (T^{clm}_{N_p} Y^{GCI}_{N_p} \prod_{q=K+1}^{p} T^{clmr}_{N'_q}) \qquad (8)$$

I^{left}_{PCC} and Y^{left}_{PCC} in Fig. 2(a) can then be calculated as $I^{left}_{N'_0}$ and $Y^{left}_{N'_0}$, respectively. A sufficient yet not necessary condition for stability of I_g can be derived based on item 1) of lemma 1 and (8), shown as follows.

Lemma 2: I_g is stable, if

1) Y^{left}_{PCC} is stable, i.e., $\forall p, q \in [1, M]$, $T^{clm}_{N_p}$ and $T^{clmr}_{N'_q}$ do not have RHP poles; and

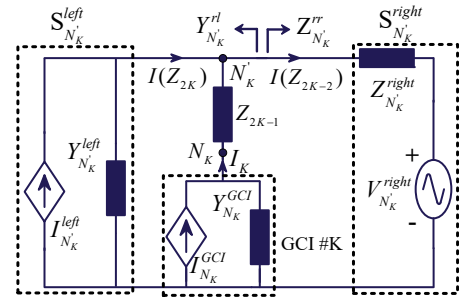

FIGURE 4. Components aggregated at both sides of node N'_K.

2) The Nyquist plot of T^{m1}_{PCC} does not encircle $(-1, j0)$.

On the other hand, the components aggregation procedure of Fig. 1 from right to left is shown in Fig. 3(b), which consists of three main steps at each node. Take node N'_K ($K \in [1, M]$) as an example. In step 1, $S^{lr}_{N'_{K-1}}$ and Z_{2K-2} are aggregated as $S^{right}_{N'_K}$ (The superscript lr means that $S^{lr}_{N'_{K-1}}$ is the aggregated sub-module by seeing rightward at the left side of node N'_{K-1}. In step 2, GCI #K and Z_{2K-1} are aggregated as $S^{bot}_{N'_K}$. In step 3, $S^{right}_{N'_K}$ and $S^{bot}_{N'_K}$ are aggregated as $S^{lr}_{N'_K}$. In addition to the parameters of $S^{bot}_{N'_K}$ shown in (5), the parameters of $S^{right}_{N'_K}$ and $S^{lr}_{N'_K}$ are calculated as

$$V^{right}_{N'_K} = V^{lr}_{N'_{K-1}}$$
$$Z^{right}_{N'_K} = Z^{lr}_{N'_{K-1}} + Z_{2K-2} \qquad (9)$$

and

$$V^{lr}_{N'_K} = T^{clml}_{N'_K} (V^{right}_{N'_K} + Z^{right}_{N'_K} I^{bot}_{N'_K})$$
$$Z^{lr}_{N'_K} = T^{clml}_{N'_K} Z^{right}_{N'_K} \qquad (10)$$

, respectively, where $T^{clml}_{N'_K} = (1 + Z^{right}_{N'_K} Y^{bot}_{N'_K})^{-1}$. The Thevenien equivalent circuit of the right part of node N'_K ($K \in [1, M]$) in Fig. 1 can then be derived based on Fig. 3(b), (5), and (9)-(10) using recursive method, shown as

$$V^{right}_{N'_K} = T^{clml}_{N'_0} V_g \prod_{q=1}^{K} T^{clml}_{N'_q} + \sum_{p=1}^{K} (T^{clm}_{N_p} I^{GCI}_{N_p} (Z_{2p-2}$$

$$+ Z^{right}_{N'_{p-1}}) \prod_{q=p}^{K} T^{clml}_{N'_q})$$

$$Z^{right}_{N'_K} = Z_g \prod_{q=0}^{K} T^{clml}_{N'_q} + \sum_{p=1}^{K} (Z_{2p-2} \prod_{q=p}^{K} T^{clml}_{N'_q}) \qquad (11)$$

Based on the derived Norton and Thevenin equivalent circuits of the left and right parts of node N'_K in (8) and (11), respectively, Fig. 1 can be simplified as Fig. 4 at node N'_K, which can further be simplified as Fig. 2(b). The parameters of $S^{right}_{N_K}$ can thus be calculated as

$$V^{right}_{N'_K} = T^{clmrl}_{N'_K} (V^{right}_{N'_K} + Z^{right}_{N'_K} I^{left}_{N'_K})$$
$$Z^{right}_{N_K} = T^{clmrl}_{N'_K} Z^{right}_{N'_K} + Z_{2K-1} \qquad (12)$$

where $T_{N'_K}^{clmrl} = (1 + Z_{N'_K}^{right} Y_{N'_K}^{left})^{-1}$. $P(Z_{N_K}^{right})$ can be calculated as

$$P(Z_{N_K}^{right}) = P(Z_{N'_K}^{right}) + P(Y_{N'_K}^{left}) + N_{(-1,j0)}(T_{N'_K}^{mrl}) \quad (13)$$

where $T_{N'_K}^{mrl} = Z_{N'_K}^{right} Y_{N'_K}^{left}$. A sufficient yet not necessary condition for stability of I_K can be derived based on item 2) of lemma 1, (8), (11), and (13), shown as follows.

Lemma 3: I_K is stable, if

1) $Y_{N'_K}^{left}$ is stable, i.e., $\forall p, q \in [K+1, M]$, $T_{N_p}^{clm}$ and $T_{N'_q}^{clmr}$ do not have RHP poles; and

2) $Z_{N'_K}^{right}$ is stable, i.e., $\forall p, q \in [1, K-1]$, $T_{N_p}^{clm}$ and $T_{N'_q}^{clml}$ do not have RHP poles; and

3) The Nyquist plot of $T_{N'_K}^{mrl}$ does not encircle $(-1, j0)$; and

4) The Nyquist plot of $T_{N_K}^{m1}$ does not encircle $(-1, j0)$.

To not lose the generality, Fig. 5(a) shows a complicated grid-connected power plant with multiple strings. Similar with the stability analysis of I_g and I_K ($K \in [1, M]$) in Fig. 1, which needs to calculate Y_{PCC}^{left} in Fig. 2(a) and $Z_{N_K}^{right}$ ($K \in [1, M]$) in Fig. 2(b), respectively, the stability analysis of grid current and output currents of all GCIs in Fig. 5(a) also needs the corresponding aggregated admittance and impedance frequency responses, respectively. Take the stability analysis of I_g and I_{12} as an example. First, a main components aggregation path is selected, shown as the red line in Fig. 5(a), based on which the rest of the whole system can be divided into strings (i.e., strings #1, #3, #5, #6, and #7) and individual GCIs (i.e., GCIs #2, #4, and #8). Then, the equivalent circuit model of Fig. 5(a) can be established in Fig. 5(b) by applying the components aggregation procedure in Fig. 3(a) to represent the five strings as five Norton equivalent circuits. Fig. 5(b) is in the similar form of Fig. 1, which indicates that Y_{PCC}^{left} and $Z_{N'_1}^{right}$ in Fig. 5(b) can be calculated using (8) and (12), respectively. Furthermore, the equivalent circuit model of sting #1 can be established as Fig. 5(c) using the derived $V_{N'_1}^{right}$ and $Z_{N'_1}^{right}$, based on which $Z_{N'_{11}}^{right}$ can be calculated using Fig. 4. It can be seen that the presented components aggregation procedures in Fig. 3 are the basis for stability analysis of more complicated grid-connected power plants.

B. PRESENTED GLOBAL STABILITY ANALYSIS AND OSCILLATION ORIGIN LOCATION METHOD

The converse-negative propositions of lemmas 2 and 3 can be derived as lemmas 4 and 5, respectively.

Lemma 4: If I_g is unstable, then

1) $\exists p, q \in [1, M]$, $T_{N_p}^{clm}$ or $T_{N'_q}^{clmr}$ has at least one pair of RHP poles; or

2) The Nyquist plot of T_{PCC}^{m1} encircles $(-1, j0)$.

Lemma 5: If I_K is unstable, then

1) $Y_{N'_K}^{left}$ is unstable, i.e., $\exists p, q \in [K+1, M]$, $T_{N_p}^{clm}$ or $T_{N'_q}^{clmr}$ has at least one pair of RHP poles; or

2) $Z_{N'_K}^{right}$ is unstable, i.e., $\exists p, q \in [1, K-1]$, $T_{N_p}^{clm}$ or $T_{N'_q}^{clml}$ has at least one pair of RHP poles; or
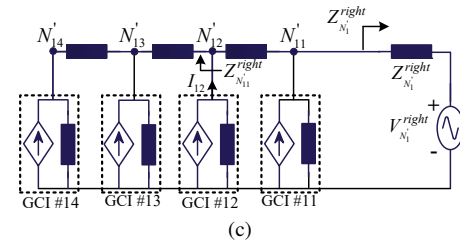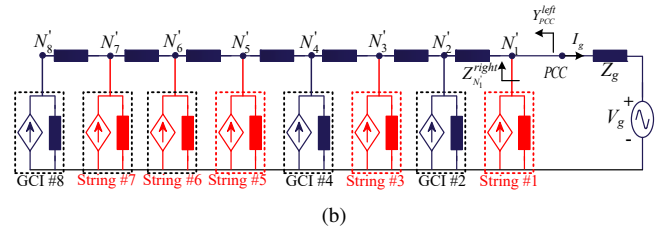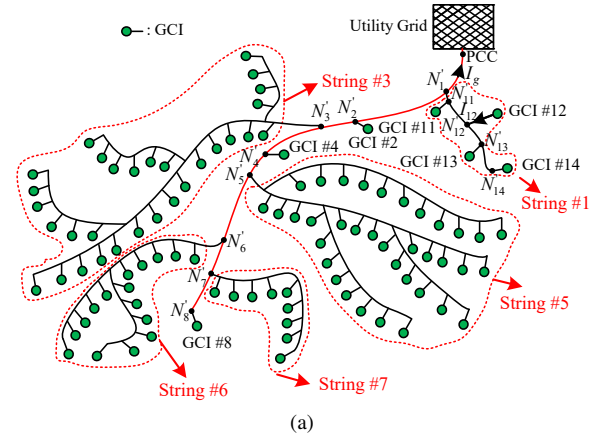

FIGURE 5. Equivalent circuit model of a complicated grid-connected power plant with multiple strings. (a) Topology of the grid-connected power plant. (b) First equivalent circuit model. (c) Second equivalent circuit model.

3) The Nyquist plot of $T_{N'_K}^{mrl}$ encircles $(-1, j0)$; or

4) The Nyquist plot of $T_{N_K}^{m1}$ encircles $(-1, j0)$.

Items 1) and 2) of lemma 1 show that Z_{PCC}^{right} and Y_{PCC}^{left} are needed for calculation of $P(I_g)$, and $Z_{N_K}^{right}$ and $Y_{N_K}^{left}$ are needed for calculation of $P(I_K)$, respectively. The derivation procedure of these impedance/admittance models in the conventional IBSCs can be explained as follows [14], [17], [19], [23]. Figs. 3(a) and 3(b) are performed to sequentially establish the Norton and Thevenin equivalent circuits of the left and right parts of nodes N'_M–N'_0 and N'_0–N'_M, respectively. On its basis, the derived Norton and Thevenin equivalent circuits at two sides of node N'_K ($K \in [1, M]$), i.e., $S_{N'_K}^{left}$ and $S_{N'_K}^{right}$ in Fig. 4, are further aggregated as $S_{N_K}^{right}$. The conventional IBSCs suffer from the following three drawbacks. First, derivations of the analytical expressions of Z_{PCC}^{right}, Y_{PCC}^{left}, $Z_{N_K}^{right}$, and $Y_{N_K}^{left}$ for RHP poles calculation may be impossible due to the industry secrecy. Second, $Z_{N_K}^{right}$ is obtained by further aggregating $S_{N'_K}^{left}$ and $S_{N'_K}^{right}$, which may be tedious and bring in heavy computational burdens. Third, the oscillation origin is difficult to locate, since it is
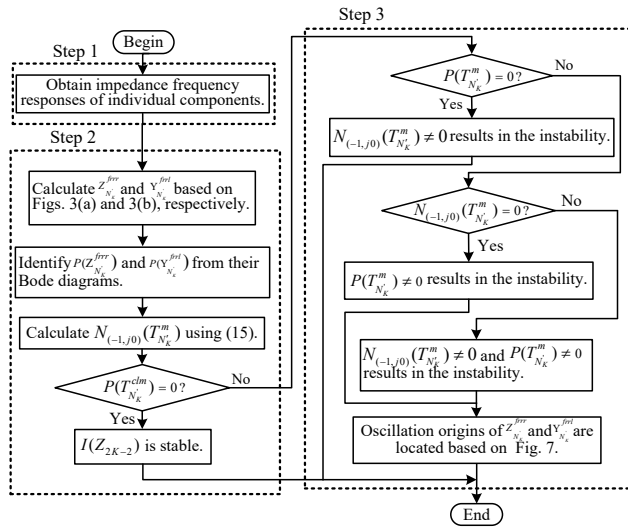
FIGURE 6. Flowchart of the presented stability analysis and oscillation origin location method at node N'_K ($K \in [1, M]$).

missing in the aggregated load and source sub-modules. For example, (13) and lemma 5 show that RHP poles of $Z_{N_K}^{right}$ can always be assumed to result from the aggregation of $Y_{N'_K}^{left}$ and $Z_{N'_K}^{right}$. This assumption may not be true, since the RHP poles of $Z_{N_K}^{right}$ may result from the inherent instability of $Y_{N'_K}^{left}$ or $Z_{N'_K}^{right}$.

According to the Kirchhoff's Law, I_K in Fig. 4 can be expressed as

$$I_K = I(Z_{2K-2}) - I(Z_{2K}) \tag{14}$$

which indicates that stability of I_K can be revealed by stability of $I(Z_{2K-2})$ and $I(Z_{2K})$, i.e., implementation point of the NC can be moved from node N_K in the existing IBSCs to the right side of node N'_K. In this case, only $Y_{N'_K}^{rl}$ and $Z_{N_K}^{rr}$ in Fig. 4 should be calculated without further calculating $Z_{N_K}^{right}$, which can release computational burdens. On its basis, Fig. 6 shows the flowchart of the presented stability analysis and oscillation origin location method at node N'_K ($K \in [1, M]$).

In step 1, impedance frequency responses of individual components are obtained, which can be achieved using the following methods. First, the system planner can theoretically derive the impedance models of the GCIs if internal control structures and parameters are provided by the vendors [3], [8], [10], [16], [17], [19]. Second, when detailed information of the GCIs is confidential for the system planner due to the industry secrecy and intellectual property protection, the vendors tend to deliver lookup tables which provide discrete impedance/admittance frequency responses of the GCIs [18], [22], [23]. Third, when black-box simulation models are provided by the manufactures, the system planner can perform frequency scanning in commercial softwares, e.g., PSCAD/EMTDC and Matlab/Simulink [26], [27], [39], [41]. For example, the impedance frequency responses of the GCIs obtained by frequency scanning are plotted in Fig.

8(b). Finally, if both discrete impedance frequency responses and black-box simulation models are not provided by the vendors, the system planner can experimentally measure the impedance frequency responses of the GCIs by successively connecting these GCIs with a configurable strong grid [42]–[44]. It is not necessary to equip a lot of measurement devices in the network.

In step 2, frequency responses of $Z_{N'_K}^{rr}$ and $Y_{N'_K}^{rl}$, i.e., $Z_{N'_K}^{frrr}$ and $Y_{N'_K}^{frrl}$, are calculated according to the components aggregation procedures in Figs. 3(a) and 3(b), respectively. On its basis, the stability of $I(Z_{2K-2})$ is assessed by

$$P(I(Z_{2K-2})) = P(T_{N'_K}^{clm}) = P(T_{N'_K}^m) + N_{(-1,j0)}(T_{N'_K}^m) \tag{15}$$

where $T_{N'_K}^{clm} = (1 + Z_{N'_K}^{frrr} Y_{N'_K}^{frrl})^{-1}$ and $T_{N'_K}^m = Z_{N'_K}^{frrr} Y_{N'_K}^{frrl}$. $P(Z_{N'_K}^{frrr})$ and $P(Y_{N'_K}^{frrl})$ are directly identified from $Z_{N'_K}^{frrr}$ and $Y_{N'_K}^{frrl}$ without knowing analytical expressions of $Z_{N'_K}^{frrr}$ and $Y_{N'_K}^{frrl}$, respectively. In detail, the magnitude-frequency curve's one peak whose phase angle is not within $[-90^o, 90^o]$ corresponds to a pair of RHP poles. If $P(T_{N'_K}^m)$ is zero, $I(Z_{2K-2})$ is stable, and no oscillation origin should be located. Otherwise, step 3 should be performed to locate the oscillation origin.

Similar with lemmas 4 and 5, the following lemma can be derived from (15).

Lemma 6: If $I(Z_{2K-2})$ is unstable, then

1) $P(Y_{N'_K}^{frrl}) \neq 0$, i.e., $\exists p \in [K, M]$, $T_{N_p}^{clm}$ has at least one pair of RHP poles, or $\exists q \in [K+1, M]$, $T_{N'_q}^{clmr}$ has at least one pair of RHP poles; or

2) $P(Z_{N'_K}^{frrr}) \neq 0$, i.e., $\exists p, q \in [1, K-1]$, $T_{N_p}^{clm}$ or $T_{N'_q}^{clml}$ has at least one pair of RHP poles; or

3) The Nyquist plot of $T_{N'_K}^m$ encircles $(-1, j0)$.

In step 3, oscillation origin of $I(Z_{2K-2})$ is located based on lemma 6. In detail, if both $Y_{N'_K}^{frrl}$ and $Z_{N'_K}^{frrr}$ do not have RHP poles, the oscillation phenomenon only results from the unstable impedance interaction between the two sub-modules. If the RHP poles exit, encirclement number of the Nyquist plot of $T_{N'_K}^m$ around $(-1, j0)$ should be counted. In detail, if the encirclement number is zero, the oscillation phenomenon only results from the inherent instability of the two sub-modules. Otherwise, the oscillation phenomenon results from both unstable impedance interaction and inherent instability. The origin of the inherent instability can further be located based on Fig. 7.

Based on (5)-(7) and item 1) of lemma 6, Fig. 7(a) shows the flowchart of origin location of RHP poles of $Y_{N'_K}^{frrl}$. If $P(Y_{N'_K}^{left})$ is zero, all the RHP poles originate from $Y_{N'_K}^{bot}$. In addition, if $P(Y_{N'_K}^{left})$ is nonzero and smaller than $P(Y_{N'_K}^{frrl})$, some RHP poles only originate from $Y_{N'_K}^{bot}$, and some RHP poles only originate from $Y_{N'_K}^{left}$. Furthermore, the scenario where $P(Y_{N'_K}^{left})$ is equal to $P(Y_{N'_K}^{frrl})$ has two sub-cases. One sub-case is that $P(Y_{N'_K}^{bot})$ is zero, which indicates that all the RHP poles result from $Y_{N'_K}^{left}$. The other sub-case is

that $P(Y_{N'_K}^{bot})$ is nonzero, which indicates that some RHP poles simultaneously occur in $P(Y_{N'_K}^{bot})$ and $Y_{N'_K}^{left}$, and local instability phenomena may happen, as shown in Section IV-B. If $Y_{N'_K}^{bot}$ is assessed to have RHP poles, it can further be concluded that unstable impedance interaction occurs between Z_{2K-1} and $Y_{N_K}^{GCI}$. On the other hand, if $Y_{N'_K}^{left}$ is assessed to have RHP poles, the origin of the RHP poles can further be located as follows. If RHP poles of $Y_{N'_K}^{left}$ occur in $Y_{N'_{K+1}}^{frrl}$, the origin of the RHP poles of $Y_{N'_{K+1}}^{frrl}$ can further be located in a similar way as $Y_{N'_K}^{frrl}$ using the recursive method. Otherwise, the RHP poles occur when $Y_{N'_{K+1}}^{frrl}$ and Z_{2K} are aggregated.

Based on (5), (9), (10), and item 2) of lemma 6, $P(Z_{N'_K}^{frrr})$ can be calculated as

$$P(Z_{N'_K}^{frrr}) = P(Z_{2K-2} + Z_{N'_{K-1}}^{lr}) = P(Z_{N'_{K-1}}^{right}) + P(Y_{N'_{K-1}}^{bot})$$
$$+ N_{(-1,j0)}(Z_{N'_{K-1}}^{right} Y_{N'_{K-1}}^{bot}) \qquad (16)$$

According to (16), Fig. 7(b) shows the flowchart of origin location of RHP poles of $Z_{N'_K}^{frrr}$. If both $P(Z_{N'_{K-1}}^{right})$ and $P(Y_{N'_{K-1}}^{bot})$ are zero, all the RHP poles of $Z_{N'_K}^{frrr}$ originate from the unstable impedance interaction between $Z_{N'_{K-1}}^{right}$ and $Y_{N'_{K-1}}^{bot}$. In addition, three sub-cases exist if the sum of $P(Z_{N'_{K-1}}^{right})$ and $P(Y_{N'_{K-1}}^{bot})$ is nonzero and smaller than $P(Z_{N'_K}^{frrr})$. Specifically, if $P(Z_{N'_{K-1}}^{right})$ is zero, some RHP poles occur during aggregation of $Z_{N'_{K-1}}^{right}$ and $Y_{N'_{K-1}}^{bot}$, and some occur in $Y_{N'_{K-1}}^{bot}$. Otherwise, if $P(Y_{N'_{K-1}}^{bot})$ is nonzero, some RHP poles occur during aggregation of $Z_{N'_{K-1}}^{right}$ and $Y_{N'_{K-1}}^{bot}$, some occur in $Z_{N'_{K-1}}^{right}$, and some occur in $Y_{N'_{K-1}}^{bot}$, and if $P(Y_{N'_{K-1}}^{bot})$ is zero, some RHP poles occur during aggregation of $Z_{N'_{K-1}}^{right}$ and $Y_{N'_{K-1}}^{bot}$, and some occur in $Z_{N'_{K-1}}^{right}$. On the other hand, three sub-cases also exist if the sum of $P(Z_{N'_{K-1}}^{right})$ and $P(Y_{N'_{K-1}}^{bot})$ is same as $P(Z_{N'_K}^{frrr})$. Specifically, if $P(Z_{N'_{K-1}}^{right})$ is zero, all the RHP poles occur in $Y_{N'_{K-1}}^{bot}$. Otherwise, if $P(Y_{N'_{K-1}}^{bot})$ is nonzero, some RHP poles occur in $Z_{N'_{K-1}}^{right}$, and some occur in $Y_{N'_{K-1}}^{bot}$, and if $P(Y_{N'_{K-1}}^{bot})$ is zero, all the RHP poles occur in $Z_{N'_{K-1}}^{right}$. The origin of the RHP poles of $Z_{N'_{K-1}}^{right}$ can further be located in a similar way as $Z_{N'_K}^{frrr}$ using the recursive method.

The RHP poles of the load and source sub-modules are commonly identified from the theoretically-derived impedance/admittance formulas, which may bring in heavy computational burdens if a large number of GCIs exist or even cannot be achieved if internal information of the GCIs is confidential [15], [16], [19], [27]. Although the RHP poles can be extracted from the impedance/admittance frequency responses using the VF and MF algorithms, selection of the optimal order is still challenging [18], [22], [23]. On the other hand, step 2 of the presented method directly identifies
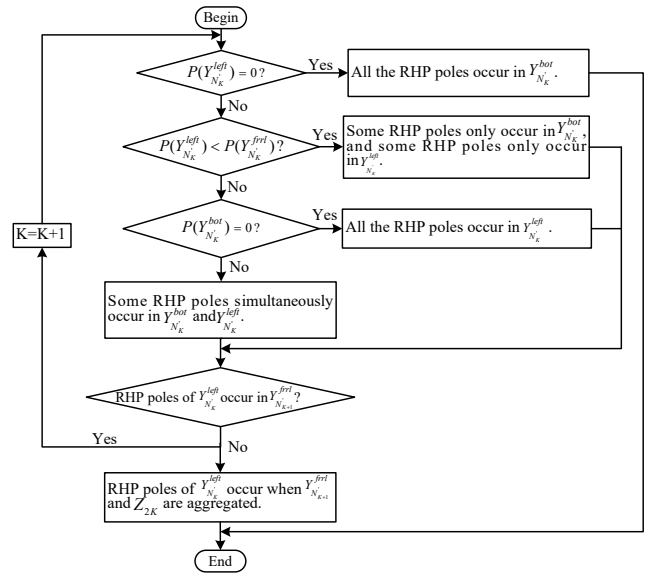
(a)
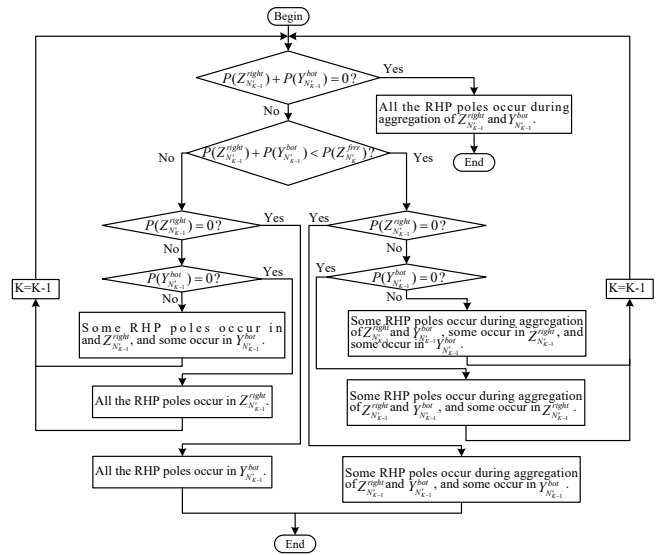
(b)

FIGURE 7. Flowcharts of origin location of RHP poles of $Y_{N'_K}^{frrl}$ and $Z_{N'_K}^{frrr}$. (a) For $Y_{N'_K}^{frrl}$. (b) For $Z_{N'_K}^{frrr}$.

the RHP poles from the impedance/admittance frequency responses, which indicates that computational burden can be released, and the black-box issue can be solved. In addition, different from the conventional NC-based stability analysis methods which use the RHP poles of the load and source sub-modules only to assess the stability at the checking nodes, the RHP poles of the load and source sub-modules are used in step 3 of the presented method to also locate the oscillation origin.
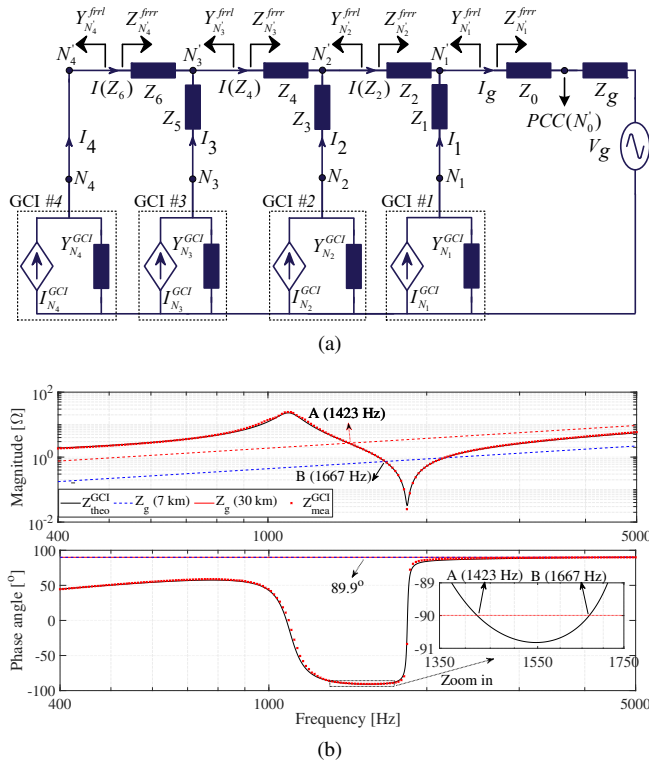
(a)

(b)

FIGURE 8. Implementation of the presented oscillation origin location method. (a) The studied four-GCI-based radial power plant. (b) Bode diagrams of the theoretical and measured impedance frequency responses of single GCI using (20) and frequency scanning scheme in [39], respectively.

IV. IMPLEMENTATION OF THE PRESENTED OSCILLATION ORIGIN LOCATION METHOD

In this section, the presented global stability analysis and oscillation origin location method is implemented in a four-GCI-based radial power plant shown in Fig. 8(a), where global stability (case 1), local instability (cases 2-4), and global instability (cases 5-8) are investigated. Circuit and controller parameters of the four GCIs are listed in Table 3 in Appendix A. In addition, lengths of the transmission lines in the eight cases are listed in Table 1. The per-unit-length (p.u.l.) resistance and inductance of theses transmission lines are 10 $\mu\Omega$/km and 10 μH/km, respectively.

According to step 1 of the proposed method in Fig. 6, the impedance frequency responses of individual GCIs in Fig. 8(a) should be obtained. 200 logarithmically-distributed frequency points between 400 Hz and 5 kHz are measured using the frequency scanning method (The detailed implementation procedure can be found in [39].). The Bode diagrams of theoretical impedance frequency responses derived by (20) and measured data are plotted as Z_{theo}^{GCI} and Z_{mea}^{GCI}, respectively, in Fig. 8(b), which shows that they highly agree with each other. Furthermore, phase angle of Z_{theo}^{GCI} is lower than -90° in frequency range (1423 Hz, 1667 Hz). When length of the transmission line is between 7 km and 30 km, the magnitudes interaction point falls into the non-passive region, and corresponding phase angles difference is higher

than 180°, which indicates that the single GCI is unstable when length of the connected transmission line is between 7 km and 30 km.

A. CASE 1: GLOBAL STABILITY

In case 1, lengths of the transmission lines in Fig. 8(a) are $l(Z_0 + Z_g) = 50$ km, $l(Z_1) = 2.5$ km, $l(Z_2) = 2$ km, $l(Z_3) = 2$ km, $l(Z_4) = 1$ km, $l(Z_5) = 1.5$ km, and $l(Z_6) = 1$ km. Bode diagrams of the four load impedances and four source admittances, i.e., $Z_{N_K'}^{frrr}$ and $Y_{N_K'}^{frrl}$ ($K \in [1,4]$) in Fig. 8(a), are plotted in Fig. 9(a), which shows an unstable peak appears at 1633 Hz of the magnitude-frequency curve of $Y_{N_1'}^{frrl}$ (A peak of the magnitude-frequency curve is unstable, if its phase angle is outside $[-90^o, 90^o]$). Therefore, $Y_{N_1'}^{frrl}$ has a pair of RHP poles whose imaginary parts are $\pm 2\pi 1633$ rad/s [18]. In addition, Nyquist diagrams of $T_{N_K'}^m$ ($K \in [1,4]$) calculated by (15) at the four checking points, i.e., the right sides of N_4'–N_1', are plotted in Fig. 9(a), which shows Nyquist plot of $T_{N_1'}^m$ encircles $(-1, j0)$ two times in anticlockwise direction. Information of the Bode and Nyquist diagrams is summarized in the table of Fig. 9(a), where Z and Y mean load and source sub-modules, respectively. According to (15), all the four checking points are stable, i.e., $I(Z_6)$, $I(Z_4)$, $I(Z_2)$, and I_g are stable. The system is globally stable, and no oscillation origin needs to be located.

Besides the oscillation origin location method presented in this article, problematic components can also be identified using conventional eigenvalue-based method and participation factor analysis. However, weak nodes with low stability margins cannot be determined intuitively. On the other hand, the Nyquist plots drawn at different nodes in this article can easily tell the system planner the stability margins of these nodes, which can provide guidelines for further stability improvement. For example, the Nyquist plots in Fig. 9(a) show that nodes N_1' and N_2' are the weakest and strongest in nodes N_4'-N_1', respectively, since the Nyquist plots of $T_{N_1'}^m$ and $T_{N_2'}^m$ are closest and farthest to $(-1, j0)$.

B. CASES 2-4: CIRCULATING CURRENT-RELATED LOCAL INSTABILITY

In case 2, lengths of the transmission lines are $l(Z_0 + Z_g) = 50$ km, $l(Z_1) = 2.5$ km, $l(Z_2) = 2$ km, $l(Z_3) = 2$ km, $l(Z_4) = 50$ km, $l(Z_5) = 20$ km, and $l(Z_6) = 20$ km. Fig. 9(b) shows an unstable peak appears at 1498 Hz of the magnitude-frequency curve of $Y_{N_3'}^{frrl}$, which indicates it has a pair of RHP poles whose imaginary parts are $\pm 2\pi 1498$ rad/s. In addition, Fig. 9(b) shows $T_{N_4'}^m$ and $T_{N_3'}^m$ encircle $(-1, j0)$ two times in clockwise and anticlockwise directions, respectively. The analysis results summarized in the table of Fig. 9(b) show that the right sides of nodes N_3'–N_1' and node N_4' are stable and unstable, respectively. Therefore, $I(Z_4)$, $I(Z_2)$, and I_g are stable, while $I(Z_6)$ oscillates at one frequency, which means circulating current exists between GCIs #4 and #3. It can be derived from step 3 of Fig. 6 and Fig. 7 that aggregations between GCI #4 and Z_6, and between

TABLE 1
SUMMARY OF THE STUDIED EIGHT CASES

| Cases	$l(Z_0+Z_g)$	$l(Z_1)$	$l(Z_2)$	$l(Z_3)$	$l(Z_4)$	$l(Z_5)$	$l(Z_6)$	$I(Z_6)$	$I(Z_4)$	$I(Z_2)$	I_g
Case 1	50 km	2.5 km	2 km	2 km	1 km	1.5 km	1 km	**Stable**	**Stable**	**Stable**	**Stable**
Case 2	50 km	2.5 km	2 km	2 km	50 km	20 km	20 km	1498 Hz	**Stable**	**Stable**	**Stable**
Case 3	100 km	2.5 km	50 km	20 km	10 km	0 km	0 km	1498 Hz	1498 Hz	**Stable**	**Stable**
Case 4	4 km	21 km	7 km	0 km	0 km	0 km	0 km	1489 Hz	1489 Hz	1489 Hz	**Stable**
Case 5	50 km	2.5 km	2 km	2 km	20 km	20 km	20 km	1441&1497 Hz	1441 Hz	1441 Hz	1441 Hz
Case 6	50 km	2.5 km	2 km	2 km	20 km	20 km	25 km	1433&1479 Hz	1433&1479 Hz	1433&1479 Hz	1433&1479 Hz
Case 7	50 km	2.5 km	2 km	2 km	50 km	20 km	25 km	1477 Hz	1477 Hz	1477 Hz	1477 Hz
Case 8	50 km	2.5 km	50 km	20 km	10 km	0 km	0 km	1443&1498 Hz	1443&1498 Hz	1443 Hz	1443 Hz
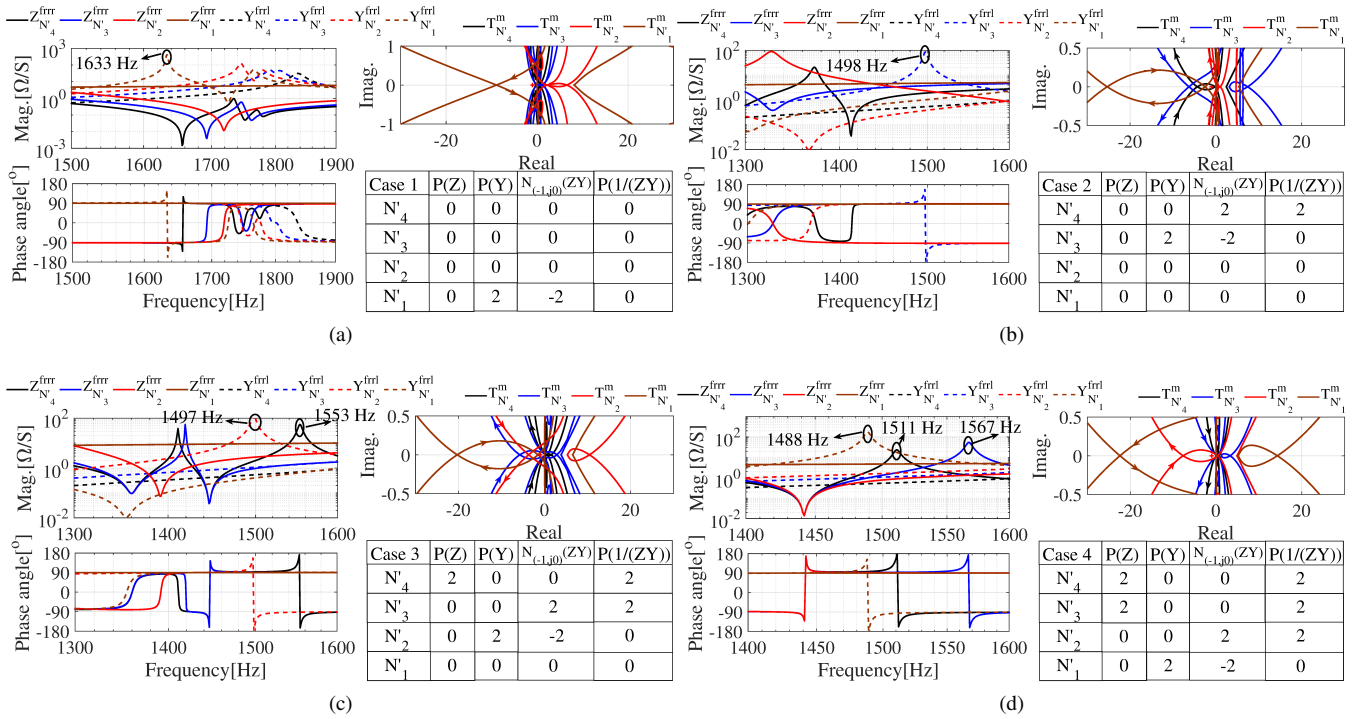
FIGURE 9. Implementation of the presented global stability analysis and oscillation origin location method in Fig. 8(a) for cases 1-4. (a) Case 1. (b) Case 2. (c) Case 3. (d) Case 4.

GCI #3 and Z_5 bring in two RHP poles in $Y_{N_3'}^{left}$ and $Y_{N_3'}^{bot}$, respectively, and the two pairs of RHP poles are overlapped, i.e., number of RHP poles of $Y_{N_3'}^{frrl}$ is reduced from 4 to 2, since the two paralleled unstable branches $Y_{N_3'}^{left}$ and $Y_{N_3'}^{bot}$ are totally same.

In case 3, lengths of the transmission lines are $l(Z_0 + Z_g) = 100$ km, $l(Z_1) = 2.5$ km, $l(Z_2) = 50$ km, $l(Z_3) = 20$ km, $l(Z_4) = 10$ km, $l(Z_5) = 0$ km, and $l(Z_6) = 0$ km, which indicates nodes N_3, N_3', N_4, and N_4' are overlapped. Fig. 9(c) shows two unstable peaks appear at 1553 Hz and 1497 Hz of the magnitude-frequency curves of $Z_{N_4'}^{frrr}$ and $Y_{N_2'}^{frrl}$, respectively, which indicates they have two pairs of RHP poles whose imaginary parts are $\pm 2\pi 1553$ rad/s and $\pm 2\pi 1497$ rad/s, respectively. In addition, Fig. 9(c) shows $T_{N_3'}^m$ and $T_{N_2'}^m$ encircle $(-1, j0)$ two times in clockwise and anticlockwise directions, respectively. The analysis results summarized in the table of Fig. 9(c) show that the right

sides of nodes $N_2'-N_1'$ and nodes $N_4'-N_3'$ are stable and unstable, respectively. Therefore, $I(Z_2)$ and I_g are stable, while $I(Z_6)$ and $I(Z_4)$ oscillate at one frequency, which means circulating current exits among GCIs #4–#2. It can be derived from step 3 of Fig. 6 and Fig. 7 that aggregations between $Y_{N_3'}^{frrl}$ and Z_4, and between GCI #2 and Z_3 bring in two RHP poles in $Y_{N_2'}^{left}$ and $Y_{N_2'}^{bot}$, respectively, and the two pairs of RHP poles are overlapped, i.e., number of RHP poles of $Y_{N_2'}^{frrl}$ is reduced from 4 to 2, since the two paralleled unstable branches $Y_{N_2'}^{left}$ and $Y_{N_2'}^{bot}$ are totally same. GCIs #4 and #3 as a whole oscillate with GCI #2, i.e., sum of harmonic contents of I_4 and I_3 is equal to harmonic content of I_2.

In case 4, lengths of the transmission lines are $l(Z_0 + Z_g) = 50$ km, $l(Z_1) = 21$ km, $l(Z_2) = 7$ km, $l(Z_3) = 0$ km, $l(Z_4) = 0$ km, $l(Z_5) = 0$ km, and $l(Z_6) = 0$ km, which indicates nodes N_2-N_4 and $N_2'-N_4'$ are overlapped. Fig. 9(d)

shows three unstable peaks appear at 1511 Hz, 1567 Hz, and 1488 Hz of the magnitude-frequency curves of $Z_{N_4'}^{frrr}$, $Z_{N_3'}^{frrr}$, and $Y_{N_1'}^{frrl}$, respectively, which indicates they have three pairs of RHP poles whose imaginary parts are $\pm 2\pi 1511$ rad/s, $\pm 2\pi 1567$ rad/s, and $\pm 2\pi 1488$ rad/s, respectively. In addition, Fig. 9(d) shows $T_{N_2'}^m$ and $T_{N_1'}^m$ encircle $(-1, j0)$ two times in clockwise and anticlockwise directions, respectively. The analysis results summarized in the table of Fig. 9(d) show that the right sides of node N_1' and nodes N_4'–N_2' are stable and unstable, respectively. Therefore, I_g is stable, while $I(Z_6)$, $I(Z_4)$, and $I(Z_2)$ oscillate at one frequency, which means circulating current exists among GCIs *#4–#1*. It can be derived from step 3 of Fig. 6 and Fig. 7 that aggregations between $Y_{N_2'}^{frrl}$ and Z_2, and between GCI *#1* and Z_1 bring in two RHP poles in $Y_{N_1'}^{left}$ and $Y_{N_1'}^{bot}$, respectively, and the two pairs of RHP poles are overlapped, i.e., number of RHP poles of $Y_{N_1'}^{frrl}$ is reduced from 4 to 2, since the two paralleled unstable branches $Y_{N_1'}^{left}$ and $Y_{N_1'}^{bot}$ are totally same. GCIs *#4–#2* as a whole oscillate with GCI *#1*, i.e., sum of harmonic contents of I_4–I_2 is equal to harmonic content of I_1.

C. CASES 5-8: GLOBAL INSTABILITY

In case 5, $l(Z_4)$ is reduced from 50 km in case 2 to 20 km. Compared with Fig. 9(b), Fig. 10(a) shows one additional unstable peak appears at 1455 Hz of the magnitude-frequency curve of $Z_{N_4'}^{frrr}$, and encirclement numbers of Nyquist plots of $T_{N_3'}^m$–$T_{N_1'}^m$ around $(-1, j0)$ in clockwise direction are increased by 2, which contributes to additional one pair of RHP poles of $T_{N_4'}^{clm}$–$T_{N_1'}^{clm}$. Therefore, $I(Z_4)$, $I(Z_2)$, and I_g oscillate at one frequency, while $I(Z_6)$ oscillates at two frequencies, which means a circulating current exists between GCIs *#4* and *#3*, and a harmonic current flows through all nodes. Based on case 2, it can be concluded that the harmonic current flowing through all nodes originates from the unstable impedance interaction at the right side of node N_3'.

In case 6, $l(Z_6)$ is increased from 20 km in case 5 to 25 km. Compared with Fig. 10(a), Fig. 10(b) shows additional unstable peaks appear at 1456 Hz, 1477 Hz, and 1474 Hz of the magnitude-frequency curves of $Y_{N_3'}^{frrl}$, $Y_{N_2'}^{frrl}$, and $Y_{N_1'}^{frrl}$, respectively, which contributes to additional one pair of RHP poles of $T_{N_3'}^{clm}$–$T_{N_1'}^{clm}$. Therefore, $I(Z_6)$, $I(Z_4)$, $I(Z_2)$, and I_g oscillate at two frequencies. It can be concluded that, the discrepancy between $l(Z_6)$ and $l(Z_5)$ enforces the circulating current between GCIs *#4* and *#3* in case 5 to flow into the rest of the power plant.

In case 7, $l(Z_6)$ is increased from 20 km in case 2 to 25 km. Compared with Fig. 9(b), Fig. 10(c) shows additional unstable peaks appear at 1457 Hz, 1477 Hz, and 1477 Hz of the magnitude-frequency curves of $Y_{N_3'}^{frrl}$, $Y_{N_2'}^{frrl}$, and $Y_{N_1'}^{frrl}$, respectively, which contributes to additional one pair of RHP poles of $T_{N_3'}^{clm}$–$T_{N_1'}^{clm}$. Therefore, $I(Z_6)$, $I(Z_4)$, $I(Z_2)$, and I_g oscillate at one frequency. It can be concluded that, the discrepancy between $l(Z_6)$ and $l(Z_5)$ enforces the circulating current between GCIs *#4* and *#3* in case 2 to flow into the rest of the power plant.

In case 8, $l(Z_0 + Z_g)$ is reduced from 100 km in case 3 to 50 km. Compared with Fig. 9(c), Fig. 10(d) shows additional unstable peaks appear at 1447 Hz and 1450 Hz of the magnitude-frequency curves of $Z_{N_4'}^{frrr}$ and $Z_{N_3'}^{frrr}$, respectively, and encirclement numbers of Nyquist plots of $T_{N_2'}^m$ and $T_{N_1'}^m$ around $(-1, j0)$ in clockwise direction are increased by 2, which contributes to additional one pair of RHP poles of $T_{N_4'}^{clm}$–$T_{N_1'}^{clm}$. Therefore, $I(Z_2)$ and I_g oscillate at one frequency, while $I(Z_6)$ and $I(Z_4)$ oscillate at two frequencies, which means a circulating current exists between GCIs *#4-#2*, and a harmonic current flows through all nodes. Based on case 3, it can be concluded that the harmonic current flowing through all nodes originates from the unstable impedance interaction at the right side of node N_1'.

The Bode and Nyquist diagrams in Figs. 9 and 10 cannot identify oscillation frequencies of the unstable cases. On the other hand, Bode diagrams of the LIMs calculated at the four checking points for cases 1-8 are plotted in Fig. 11, based on which oscillation frequencies of $I(Z_6)$, $I(Z_4)$, $I(Z_2)$, and I_g are summarized in Table 1.

V. SIMULATION AND REAL-TIME VERIFICATION

In this section, the correctness of the global stability analysis and oscillation origin location results in Section IV based on the presented method is validated by simulation results in Matlab/Simulink platform and real-time verification results in OPAL-RT platform.

A. SIMULATION VERIFICATION BASED ON MATLAB/SIMULINK PLATFORM

Fig. 12 shows time-domain simulation results of output currents of the four GCIs and grid current in Fig. 8(a) for cases 1-5. Fig. 12(a) shows simulation results when case 1 changes to case 2 at 3s, which indicates the system is globally stable before 3 s and locally unstable after 3 s. In detail, the 1500-Hz frequency components of both I_4 and I_3 in case 2 are 244 A, which indicates this harmonic current circulates between GCIs *#4* and *#3*. The analysis results in Figs. 9(a), 9(b), 11(a), 11(b), and Table 1 are thus validated.

Fig. 12(b) shows simulation results of case 3, which indicates the system is locally unstable. In detail, the 1500-Hz frequency components of both I_4 and I_3 are 682 A and half of that of I_2, which indicates this harmonic current circulates between GCI *#2* and the sub-module composed of GCIs *#4* and *#3*. The analysis results in Figs. 9(c), 11(c), and Table 1 are thus validated.

Fig. 12(c) shows simulation results of case 4, which indicates the system is locally unstable. In detail, the 1491-Hz frequency components of I_4-I_2 are 572 A and one third of that of I_1, which indicates this harmonic current circulates between GCI *#1* and the sub-module which consists of GCIs *#4–#2*. The analysis results in Figs. 9(d), 11(d), and Table 1 are thus validated. Figs. 12(a)-(c) show grid current is stable
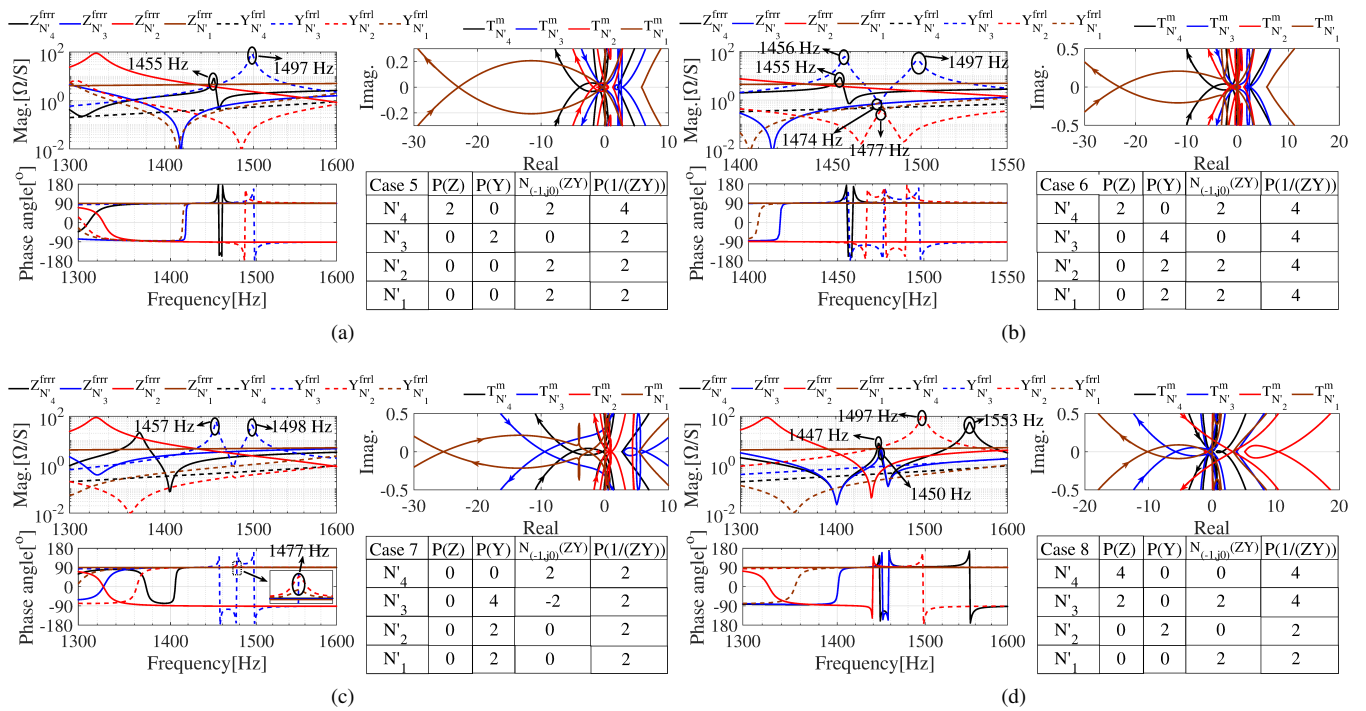
FIGURE 10. Implementation of the presented global stability analysis and oscillation origin location method in Fig. 8(a) for cases 5-8. (a) Case 5. (b) Case 6. (c) Case 7. (d) Case 8.
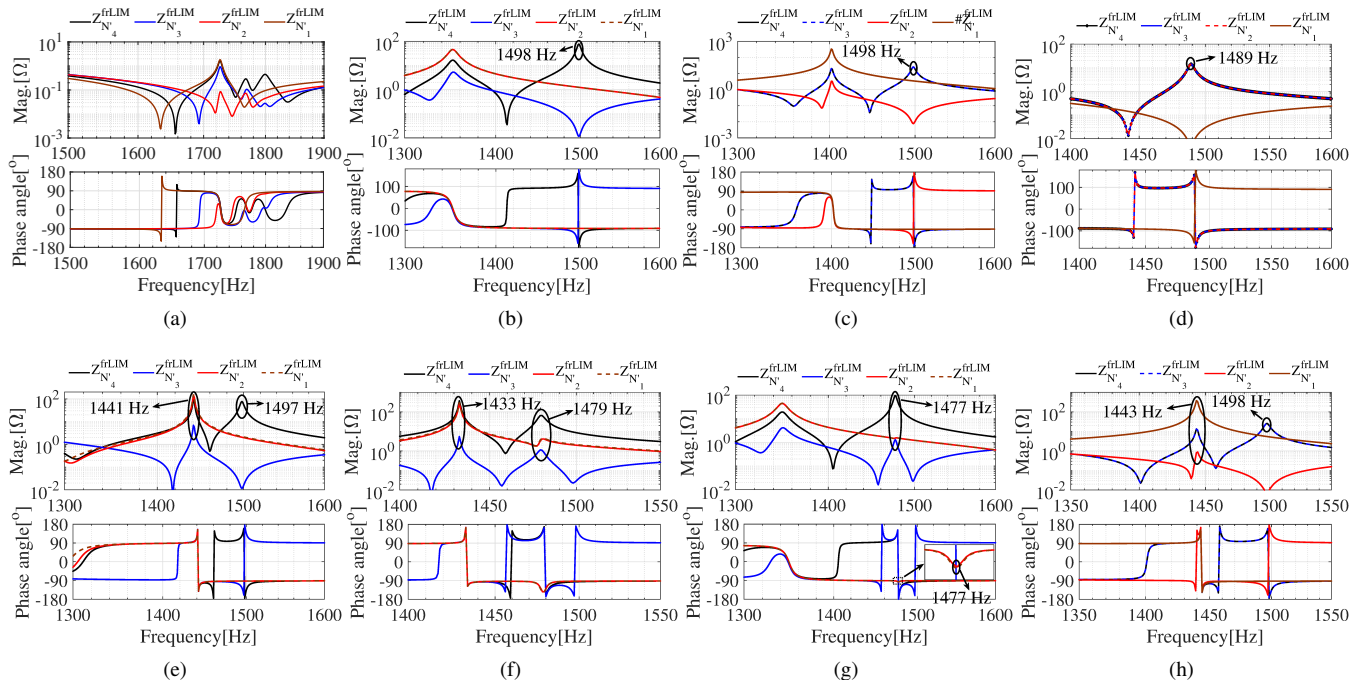

FIGURE 11. Bode diagrams of system LIMs at the four checking points in Fig. 8(a) for cases 1-8. (a) Case 1. (b) Case 2. (c) Case 3. (d) Case 4. (e) Case 5. (f) Case 6. (g) Case 7. (h) Case 8.
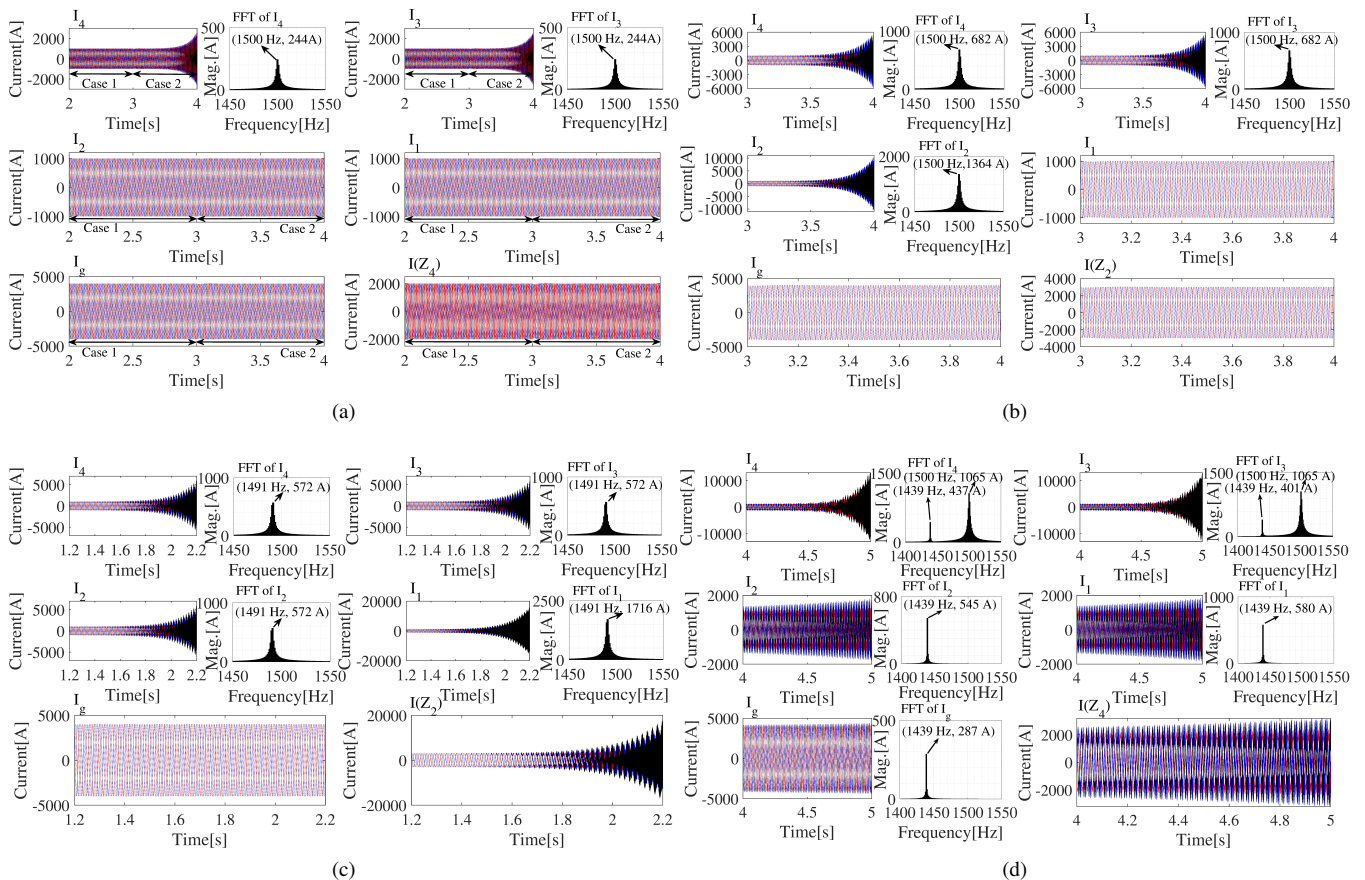
FIGURE 12. Simulation results of output currents of the four GCIs and grid current in Fig. 8(a) for cases 1-5. (a) Case 1 changes to case 2 at 3 s. (b) Case 3. (c) Case 4. (d) Case 5.

even output currents of some GCIs are unstable, which indicates stability of grid current can be enforced by installing a parallel branch which is totally the same as the unstable branch.

Fig. 12(d) shows simulation results of case 5, which indicates the system is globally unstable. In detail, the 1500-Hz frequency components of both I_4 and I_3 are 1065 A, which indicates this harmonic current circulates between GCIs #4 and #3. Furthermore, the 1439-Hz frequency components satisfy that $\mathcal{F}_{1439}(I_4 + I_3 + I_g) = \mathcal{F}_{1439}(I_2 + I_1)$, which indicates this harmonic current circulates between the sub-module composed of GCIs #4, #3 and grid and the sub-module composed of GCIs #2 and #1 ($\mathcal{F}$ indicates the FFT operator.). The analysis results in Figs. 10(a), 11(e), and Table 1 are thus validated.

B. REAL-TIME VERIFICATION BASED ON OPAL-RT PLATFORM

Fig. 13 shows picture of the real-time OPAL-RT digital simulator platform in laboratory, where OP5600 hardware platform and OPAL-RT's RT-LAB software platform are combined to validate the model developed in Matlab/Simulink platform in a real-time manner. The real-time verification results are then post-processed in Matlab software.

FIGURE 13. Picture of the real-time OPAL-RT digital simulator platform.

Fig. 14(a) shows real-time verification results of case 6, which indicates the system is globally unstable. In detail, the 1433-Hz frequency components of I_4-I_1 and I_g satisfy that $\mathcal{F}_{1433}(I_4 + I_3 + I_g) = \mathcal{F}_{1433}(I_2 + I_1)$, which indicates this harmonic current circulates between the sub-module composed of GCIs #4, #3, and grid and the sub-module composed of GCIs #2 and #1. In addition, the 1484-Hz frequency components of I_4-I_1 and I_g satisfy that $\mathcal{F}_{1484}(I_4 + I_2 + I_1) = \mathcal{F}_{1484}(I_3 + I_g)$, which indicates this harmonic current circulates between the sub-module composed of GCIs #4, #2, and #1 and the sub-module composed GCIs #3 and grid. The analysis results in Figs. 10(b), 11(f), and Table 1 are
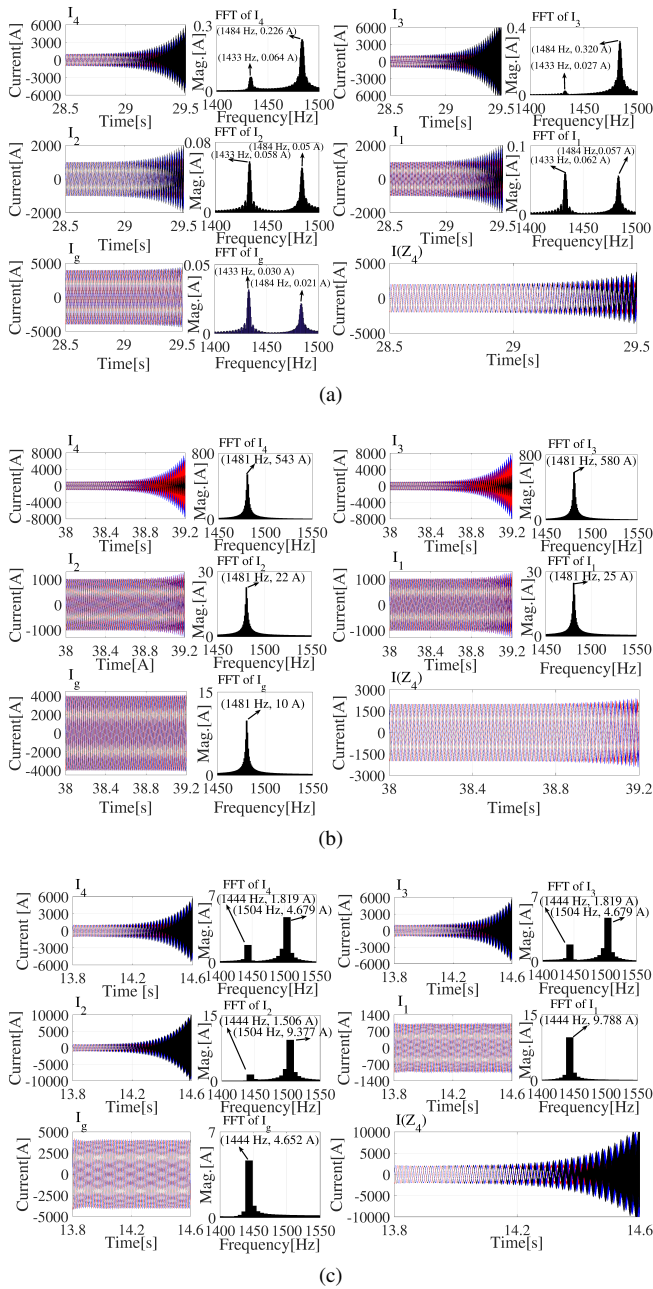
FIGURE 14. Real-time verification results of output currents of the four GCIs and grid current in Fig. 8(a) for cases 6-8. (a) Case 6. (b) Case 7. (c) Case 8.

thus validated. Since the 1484-Hz harmonic current oscillates much faster than the 1433-Hz harmonic current, only the frequency contents at initial oscillation stage from 28.5 s to 28.7 s are extracted.

Fig. 14(b) shows real-time verification results of case 7, which indicates the system is globally unstable. In detail, the 1481-Hz frequency components of I_4–I_1 and I_g satisfy that $\mathcal{F}_{1481}(I_4 + I_2 + I_1) = \mathcal{F}_{1481}(I_3 + I_g)$, which indicates this harmonic current circulates between the sub-module composed of GCIs #4, #2, and #1 and the sub-module composed of GCI #3 and grid. The analysis results in Figs. 10(c), 11(g),

and Table 1 are thus validated.

Fig. 14(c) shows real-time verification results of case 8, which indicates the system is globally unstable. In detail, the 1441-Hz harmonic currents satisfy that $\mathcal{F}_{1441}(I_4 + I_3 + I_2 + I_g) = \mathcal{F}_{1441}(I_1)$, which indicates this harmonic current circulates between the sub-module composed of GCIs #4, #3, #2, and grid and the sub-module composed of GCI #1. Furthermore, the 1504-Hz frequency components of both I_4 and I_3 are 4.679 A and half of that of I_2, which indicates this harmonic current circulates between GCI #2 and the sub-module composed of GCIs #4 and #3. The analysis results in Figs. 10(d), 11(h), and Table 1 are thus validated.

VI. DISCUSSIONS
In this section, the oscillation origin location method presented in this article is compared with the existing NC-based IBSCs. In addition, the computational burdens of the presented method when network complexity and GCIs number increase are investigated. Some other issues related with the presented method are also discussed.

A. COMPARATIVE ANALYSIS OF SEVERAL BREEDS OF NC-BASED IBSCS
Based on the components aggregation procedures in Fig. 3, several impedance aggregation methods have been reported in the existing literature, which can mainly be grouped into the following five breeds [13], [16]–[19], [23], [36]–[39], [45]–[49]. In IBSC #1, the NC is performed one time at a certain node, e.g., PCC, with calculating RHP poles of the minor loop gain (MLG) and encirclement number of its Nyquist plot around $(-1, j0)$, where the RHP poles of the MLG are identified from the theoretically-derived formulas of the load impedance and source admittance models [13], [16], [19], [45]–[47]. Different from IBSC #1, to better cope with the black-box models, the RHP poles of the MLG are identified in IBSC #2 from impedance frequency responses (IFRs) of load and source sub-modules based on the VF algorithm [18], [23]. Furthermore, to avoid calculating the RHP poles of the MLG, stability of grid current is assessed in IBSC #3 by performing the NC sequentially from farthest node to PCC [19], [36]–[39]. The grid current is assessed as stable if the Nyquist plots at all the checking nodes do not encircle $(-1, j0)$. However, only local stability, i.e., stability of grid current, can be obtained in IBSCs #1, #2, and #3. In IBSC #4, the NC is performed at all nodes to assess stability of grid current and output currents of all GCIs with calculating RHP poles of the MLGs and encirclement numbers of their Nyquist plots around $(-1, j0)$, where the RHP poles of the MLGs are identified from the theoretically-derived formulas of the load impedance and source admittance models [17], [48], [49]. In IBSC #5, the NC is performed sequentially at all nodes to assess stability of grid current and output currents of all GCIs without calculating RHP poles of the MLGs. Similar with IBSC #3, the system is assessed as globally stable if the Nyquist plots at all the checking nodes do not encircle $(-1, j0)$.
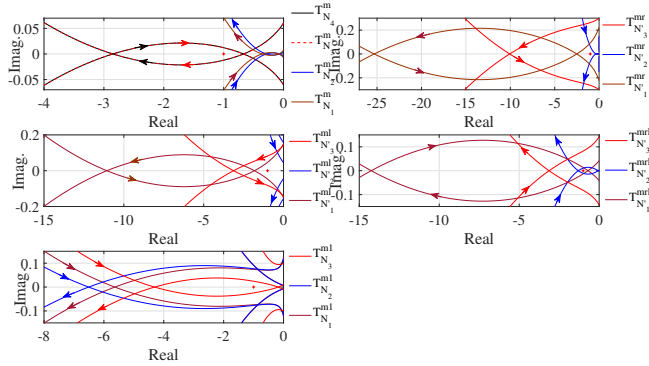
FIGURE 15. Implementation of IBSC #5 for case 2 in Fig. 8(a).

Performances of the aforementioned five breeds of IBSCs for Fig. 1 are summarized in Table 2. It can be seen that only local stability feature can be obtained by IBSCs #1, #2, and #3. Global stability feature can be obtained by IBSCs #4 and #5. However, white-box models are required in IBSC #4, and oscillation origin cannot be located. In addition, the stability analysis result obtained by IBSC #5 is conservative, and the implementation procedure is relatively complicated. Take case 2 of Fig. 8(a) as an example. When IBSCs #1-#3 are used at PCC, although stability of I_g can be successfully assessed as stable, the circulating current-related local instability of I_4 and I_3 is ignored. Furthermore, Fig. 15 shows the analysis results based on IBSC #5. The stability of I_g can be assessed based on $T_{N_4}^m$-$T_{N_1}^m$ and $T_{N_3'}^{mr}$-$T_{N_1}^{mr}$. Although $T_{N_4}^m$, $T_{N_3}^m$, and $T_{N_3'}^{mr}$ encircle $(-1, j0)$ two times in clockwise, clockwise, and anticlockwise directions, respectively, I_g in Fig. 12(a) is stable. Similar analysis can be performed for I_2 and I_1. Therefore, IBSC #5 is a sufficient yet not necessary condition for global stability.

In the presented IBSC, the NC is performed sequentially at all nodes of the checking path to assess stability of grid current and output currents of all GCIs with calculating RHP poles of the MLGs and encirclement numbers of their Nyquist plots around $(-1, j0)$, where RHP poles of the MLGs are directly identified from the IFRs. The theoretical analysis in Section IV and simulation verification in Section V show that, compared with the aforementioned five breeds of IBSCs, the presented IBSC provides a sufficient and necessary condition for global stability and can locate the oscillation origin only based on IFRs of the black-box models.

B. VARIATION OF COMPUTATIONAL BURDENS OF THE PRESENTED METHOD WITH NETWORK COMPLEXITY

To validate effectiveness of the presented oscillation origin location method for more complicated network structure, the radial power plant in Fig. 1 with eight GCIs (i.e., $M = 8$) is further investigated. Lengths of the transmission lines are $l(Z_0 + Z_g) = 2$ km, $l(Z_1) = l(Z_3) = l(Z_5) = l(Z_7) = l(Z_9) = 2.5$ km, $l(Z_2) = l(Z_4) = l(Z_6) = l(Z_8) = l(Z_{10}) = l(Z_{11}) = 2$ km, $l(Z_{12}) = 50$ km, $l(Z_{13}) = 20$ km,
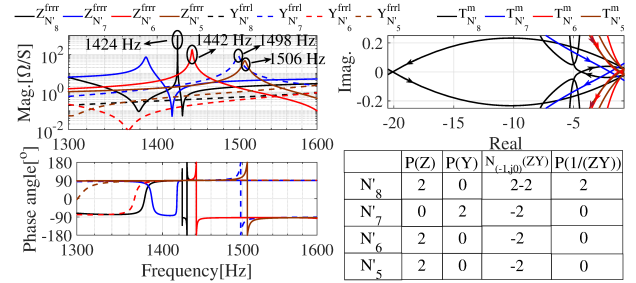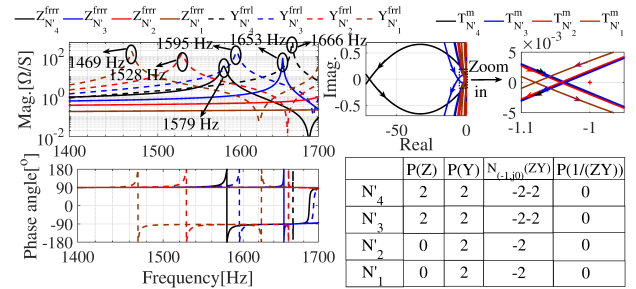
FIGURE 16. Implementation results of the presented oscillation origin location method for the eight-GCI-based power plant in Fig. 1 ($M = 8$). (a) Implementation results for nodes N_8'-N_5'. (b) Implementation results for nodes N_4'-N_1'.

and $l(Z_{14}) = 20$ km. The analysis results summarized in the tables of Fig. 16 show that the right sides of nodes N_7'–N_1' and node N_8' are stable and unstable, respectively. Therefore, $I(Z_{12})$, $I(Z_{10})$, $I(Z_8)$, $I(Z_6)$, $I(Z_4)$, $I(Z_2)$, and I_g are stable, while $I(Z_{14})$ oscillates at one frequency, which means circulating current exists between GCIs #8 and #7. It can be derived from step 3 of Fig. 6 and Fig. 7 that aggregations between GCI #8 and Z_{14}, and between GCI #7 and Z_{13} bring in two RHP poles in $Y_{N_7'}^{left}$ and $Y_{N_7'}^{bot}$, respectively, and the two pairs of RHP poles are overlapped, i.e., number of RHP poles of $Y_{N_7'}^{frrl}$ is reduced from 4 to 2, since the two paralleled unstable branches $Y_{N_7'}^{left}$ and $Y_{N_7'}^{bot}$ are totally same.

Fig. 17 shows the Matlab/Simulink-based simulation verification results of Fig. 16, which indicates I_8 and I_7 are unstable, while $I(Z_{12})$ and I_g are stable (I_6-I_1 are also stable, and their simulation results are omitted for simplicity.). The simulation results indicate that one harmonic current circulates between GCIs #8 and #7. The correctness of the analysis results in Fig. 16 is thus validated.

Furthermore, Fig. 18 shows the variations of the running times of the presented IBSC and IBSC #5 when number of the GCIs in Fig. 1 increases from 1 to 1000 with step size 10 (Intel i7-7600U processor and 8 GB of RAM). It can be seen that the running time of the presented IBSC increases linearly as number of checking nodes increases, and the average execution time for each checking node is 23.5 s/1000=23.5 ms. On the other hand, the average execution time for each checking node using IBSC #5 is 105.3 s/1000=105.3 ms, which is about four times slower than the presented IBSC.

TABLE 2
PERFORMANCE COMPARISONS OF SIX BREEDS OF IBSCS

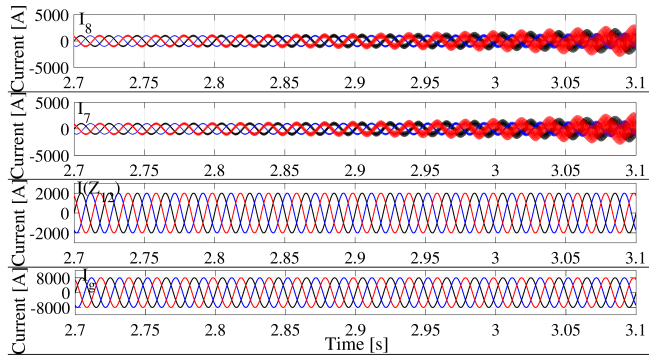| IBSCs	Implem. number	Suff. or Nec.?	Black-box model?	RHP poles cal.?	Global stability?	Oscillation origin location?
IBSC #1	1	Suff. and Nec.	No	Yes (AIM)	No	No
IBSC #2	1	Suff. and Nec.	Yes	Yes (IFRs)	No	No
IBSC #3	2M+1	Suff. not Nec.	Yes	No	No	Yes
IBSC #4	M+1	Suff. and Nec.	No	Yes (AIM)	Yes	No
IBSC #5	5M-4	Suff. not Nec.	Yes	No	Yes	Yes
Presented IBSC	M+1	Suff. and Nec.	Yes	Yes (IFRs)	Yes	Yes

FIGURE 17. Simulation verification results of Fig. 16.
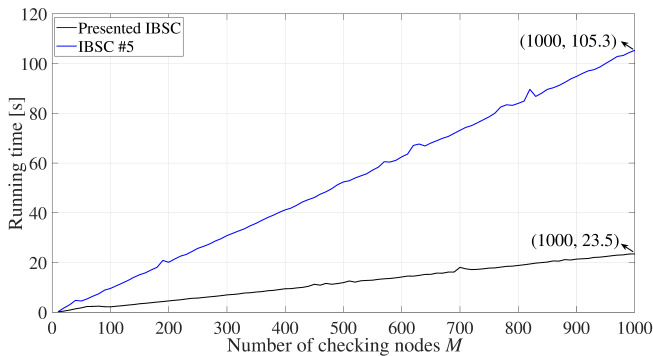

FIGURE 18. Effects of number of GCIs in Fig. 1 on running times of different NC-based stability analysis methods.

C. OTHER ISSUES RELATED WITH THE PRESENTED METHOD

It is possible to further identify the problematic controller or even controller parameters based on the identified problematic components. The discrete impedance frequency responses of the GCIs are fitted as continuous transfer functions in [18], [41], and [43] using vector fitting algorithm, system identification technique, and least-squares fitting routine, respectively, based on which the circuit and controller parameters of the GCIs are identified by equalizing the fitted transfer functions and theoretical impedance models. Note that internal structure should be known for further circuit and controller parameters identification.

This paper aims to present a global stability analysis method to identify the oscillation origin in the multiple-GCI-based power systems, where the effects of various control

loops on system stability are not focused. Therefore, the digital time delay-related high-frequency stability issue, as a representative, is used to verify the validity of the proposed method in this paper. The DC-link voltage dynamics are, thus, neglected by assuming a large DC-link capacitor. In fact, similar simplification has been widely adopted in existing works. For example, the dynamics of DC-link voltage control and PLL are neglected in [31], [40], where high-frequency harmonic instability is focused. In addition, the DC-link voltage is assumed as constant in [45] to focus on the PLL-related low-frequency instability issue. The detailed impedance modeling procedure of PMSG considering DC-link voltage dynamics can be found in [50].

When outer controller dynamics cannot be ignored, the presented three-step-based oscillation origin location method in Fig. 6 can be modified for further low-frequency stability analysis. In step 1, the MIMO instead of SISO impedance/admittance frequency responses of GCIs are measured, as shown in the authors' recent work [39]. On its basis, the MIMO impedance/admittance frequency responses of the aggregated load and source sub-modules are derived still using Fig. 3, except that the SISO impedance/admittance models in (5)-(7) and (9)-(10) are updated as the corresponding MIMO impedance/admittance models. In step 2, similar with the identification method in this article, the RHP poles of the load and source sub-modules are directly identified from their MIMO impedance and admittance frequency responses, respectively. In addition, the generalized NC is applied on the ratio of the MIMO impedance frequency responses of the load and source sub-modules. In step 3, the oscillation origin location based on the MIMO impedance/admittance frequency responses can be achieved in a similar way as Fig. 7, since the RHP poles generation mechanism during components aggregation procedure using the SISO and MIMO impedance models are the same.

VII. CONCLUSION

This article presents a global stability analysis and oscillation origin location method of multiple-GCI-based power systems. Based on terminal impedance frequency responses of individual components, frequency responses of equivalent load and source sub-modules are calculated at all nodes along the selected components aggregation path, based on which RHP poles are directly identified from Bode diagrams of the load and source frequency responses without knowing analytical expressions. Stability features of these nodes and oscillation origin can further be obtained based on the im-
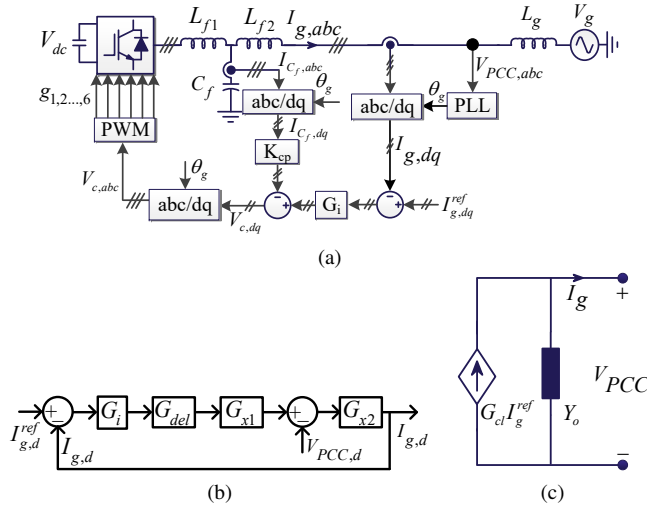
This article has been accepted for publication in a future issue of this journal, but has not been fully edited. Content may change prior to final publication. Citation information: DOI 10.1109/OJIES.2020.3045620,
IEEE Open Journal of the Industrial Electronics Society

Zhou *et al.*: Electromagnetic Oscillation Origin Location

(a)

(b)

(c)

FIGURE 19. Topology and control block diagram of an LCL-filtered GCI under grid current control mode. (a) Control structure. (b) d-axis control block diagram. (c) Norton equivalent circuit of the GCI.

proved IBSC. Effectiveness of the presented oscillation origin location method is validated by theoretical analysis, simulation results in Matlab/Simulink platform, and real-time verification in OPAL-RT platform. The presented method can assess global stability and locate oscillation origin location more efficiently. Furthermore, local instability issues induced by impedance/admittance order reduction phenomena when paralleled branches are totally the same and unstable can also be identified. Inspired by this, one future work can be to improve stability of grid current by enforcing the paralleled branch to be the same as the existing unstable branch.

.

APPENDIX A RELATION BETWEEN RHP POLES OF CURRENT SOURCE AND ADMITTANCE OF NORTON EQUIVALENT CIRCUIT OF GCIS

Fig. 19(a) shows the control strategy of an LCL-filtered GCI under grid current control mode with PLL synchronization. The circuit and controller parameters of the GCI are listed in Table 3. The impedance/admittance model of the GCI is an MIMO matrix when considering PLL dynamics [3], [10], [16]. However, PLL only shapes low-frequency impedance/admittance characteristics of the GCI [3], [10]. In addition, the influence of PLL can be ignored if its bandwidth is narrow enough. In this case, d-axis and q-axis impedance components are decoupled, and d-axis impedance component suffices for stability analysis. In fact, similar simplification has been widely adopted in existing work [4], [14], [18], [22], [23], [30], [31], [37], [40]. The d-axis control block diagram can be derived as Fig. 19(b), where $G_i = K_p + \frac{K_i}{s}$ is the current controller, and $G_{del} = e^{-1.5T_s s}$ represents the digital time delay. In addition, G_{x1} and G_{x2} are expressed as

$$G_{x1} = \frac{1}{L_{f1}C_f s^2 + C_f K_{cp} G_{del} s + 1} \quad (17)$$

and

$$G_{x2} = \frac{L_{f1}C_f s^2 + C_f K_{cp} G_{del} s + 1}{L_{f1}L_{f2}C_f s^3 + L_{f2}C_f K_{cp} G_{del} s^2 + (L_{f1} + L_{f2})s} \quad (18)$$

, respectively. On its basis, the closed-loop transfer function G_{cl} and output admittance Y_o can be calculated as

$$G_{cl} = \frac{I_{g,d}}{I_{g,d}^{ref}} = \frac{G_i G_{del} G_{x1} G_{x2}}{1 + G_i G_{del} G_{x1} G_{x2}} \quad (19)$$

and

$$Y_o = -\frac{I_{g,d}}{V_{PCC,d}} = \frac{G_{x2}}{1 + G_i G_{del} G_{x1} G_{x2}} \quad (20)$$

, respectively. Based on (20), $I_{g,d}$ can be derived as

$$I_{g,d} = G_{cl} I_{g,d}^{ref} - Y_o V_{PCC,d} \quad (21)$$

Therefore, the Norton equivalent circuit of the GCI can be established as Fig. 19(c). It can be seen from (19) and (20) that $G_{cl} = G_i G_{del} G_{x1} Y_o$. Since G_i, G_{del}, and G_{x1} are designed to not have RHP poles, the current source $G_{cl} I_g^{ref}$ and admittance Y_o in Fig. 19(c) share the same stability characteristics. Therefore, $I_{N_K}^{left} = \frac{N(I_{N_K}^{left})}{D_1(I_{N_K}^{left})D_2(I_{N_K}^{left})}$ and $Y_{N_K}^{left} = \frac{N(Y_{N_K}^{left})}{D_1(Y_{N_K}^{left})D_2(Y_{N_K}^{left})}$ can be assumed in Fig. 2(b), where $D_1(I_{N_K}^{left}) = D_1(Y_{N_K}^{left})$ are the shared RHP poles of $I_{N_K}^{left}$ and $Y_{N_K}^{left}$. Note that $I_{N_K}^{left}$ and $Y_{N_K}^{left}$ are commonly designed to not have RHP poles.

TABLE 3
CIRCUIT AND CONTROLLER PARAMETERS OF THE GCI IN FIG. 19(A)

Parameter	Value
DC-link voltage V_{dc}	1150 V
Grid voltage (phase-to-phase RMS) V_g	575 V
Grid fundamental angular frequency ω_1	314 rad/s
Inverter-side filter inductance L_{f1}	0.5 mH
Grid-side filter inductance L_{f2}	0.2 mH
Filter capacitance C_f	50 μF
Capacitor-current-feedback coefficient K_{cp}	0.6 Ω
Switching frequency f_{sw}	2.5 kHz
Sampling frequency f_s	10 kHz
Proportional gain of current controller K_p	1.2 Ω
Integral gain of current controller K_i	65 Ω/s
Proportional gain of PLL K_{ppll}	2 rad/(Vs)
Integral gain of PLL K_{ipll}	2 rad/(Vs^2)
Current reference value $I_{g,d}^{ref}$	1.0 kA
Current reference value $I_{g,q}^{ref}$	0 A

APPENDIX B DERIVATION OF $P(I_G)$, $P(I_K)$, AND $P(Z_{N_K}^{RIGHT})$

Based on Appendix A, (8) shows that I_{PCC}^{left} and Y_{PCC}^{left} share the same RHP poles. Assume that $I_{PCC}^{left} = \frac{N(I_{PCC}^{left})}{D_1(I_{PCC}^{left})D_2(I_{PCC}^{left})}$ and $Y_{PCC}^{left} = \frac{N(Y_{PCC}^{left})}{D_1(Y_{PCC}^{left})D_2(Y_{PCC}^{left})}$, where $D_1(I_{PCC}^{left}) = D_1(Y_{PCC}^{left})$ are the shared RHP poles of I_{PCC}^{left} and Y_{PCC}^{left}. Therefore, (1) can be reformulated as

$$I_g = \frac{D_2(Y_{PCC}^{left})N(I_{PCC}^{left}) - D_2(I_{PCC}^{left})V_g N(Y_{PCC}^{left})}{D_2(I_{PCC}^{left})(D_1(Y_{PCC}^{left})D_2(Y_{PCC}^{left}) + Z_g N(Y_{PCC}^{left}))} \quad (22)$$

This article has been accepted for publication in a future issue of this journal, but has not been fully edited. Content may change prior to final publication. Citation information: DOI 10.1109/OJIES.2020.3045620, IEEE Open Journal of the Industrial Electronics Society

Zhou *et al.*: Electromagnetic Oscillation Origin Location

Since $D_2(I_{PCC}^{left})$ does not have RHP zeros, $P(I_g)$ can be calculated as

$$P(I_g) = Z(D_1(Y_{PCC}^{left})D_2(Y_{PCC}^{left}) + Z_g N(Y_{PCC}^{left}))$$
$$= Z(1 + Z_g Y_{PCC}^{left}) = Z(1 + Z_{PCC}^{right} Y_{PCC}^{left}) \quad (23)$$

Therefore, (3) is proved. Similarly, (12) shows that $V_{N_K}^{right}$ and $Z_{N_K}^{right}$ share the same RHP poles. Assume that $V_{N_K}^{right} = \frac{N(V_{N_K}^{right})}{D_1(V_{N_K}^{right})D_2(V_{N_K}^{right})}$ and $Z_{N_K}^{right} = \frac{N(Z_{N_K}^{right})}{D_1(Z_{N_K}^{right})D_2(Z_{N_K}^{right})}$, where $D_1(V_{N_K}^{right}) = D_1(Z_{N_K}^{right})$ are the shared RHP poles of $V_{N_K}^{right}$ and $Z_{N_K}^{right}$. Therefore, (2) can be reformulated as

$$I_K = (N(I_{N_K}^{left})D_1(Z_{N_K}^{right})D_2(Z_{N_K}^{right})D_2(Y_{N_K}^{left})D_2(V_{N_K}^{right})$$
$$-D_2(I_{N_K}^{left})N(V_{N_K}^{right})N(Y_{N_K}^{left})D_2(Z_{N_K}^{right}))/(D_2(I_{N_K}^{left})$$
$$D_2(V_{N_K}^{right})(D_1(Z_{N_K}^{right})D_2(Z_{N_K}^{right})D_1(Y_{N_K}^{left})D_2(Y_{N_K}^{left})$$
$$+N(Z_{N_K}^{right})N(Y_{N_K}^{left}))) \quad (24)$$

Since $D_2(I_{N_K}^{left})$ and $D_2(V_{N_K}^{right})$ do not have RHP zeros, $P(I_K)$ can be calculated as

$$P(I_K) = Z(D_1(Z_{N_K}^{right})D_2(Z_{N_K}^{right})D_1(Y_{N_K}^{left})D_2(Y_{N_K}^{left})$$
$$+N(Z_{N_K}^{right})N(Y_{N_K}^{left})) = Z(1 + Z_{N_K}^{right} Y_{N_K}^{left}) (25)$$

Therefore, (4) is proved. Assume that $Z_{N_{K-1}'}^{right} = \frac{N(Z_{N_{K-1}'}^{right})}{D(Z_{N_{K-1}'}^{right})}$ and $Y_{N_{K-1}'}^{bot} = \frac{N(Y_{N_{K-1}'}^{bot})}{D(Y_{N_{K-1}'}^{bot})}$. According to (10), $Z_{N_{K-1}'}^{lr}$ can be calculated as

$$Z_{N_{K-1}'}^{lr} = \frac{N(Z_{N_{K-1}'}^{right})D(Y_{N_{K-1}'}^{bot})}{D(Z_{N_{K-1}'}^{right})D(Y_{N_{K-1}'}^{bot}) + N(Z_{N_{K-1}'}^{right})N(Y_{N_{K-1}'}^{bot})} \quad (26)$$

Therefore, $P(Z_{N_{K-1}'}^{lr})$ can be calculated as

$$P(Z_{N_{K-1}'}^{lr}) = Z(D(Z_{N_{K-1}'}^{right})D(Y_{N_{K-1}'}^{bot}) + N(Z_{N_{K-1}'}^{right})N(Y_{N_{K-1}'}^{bot}))$$
$$= Z(1 + Z_{N_{K-1}'}^{right} Y_{N_{K-1}'}^{bot}) = P(Z_{N_{K-1}'}^{right}) + N_{(-1,j0)}(Z_{2K-3}Y_{N_{K-1}'}^{GCI}$$
$$+N_{(-1,j0)}(Z_{N_{K-1}'}^{right} Y_{N_{K-1}'}^{bot}) \quad (27)$$

Therefore, (13) is proved. It can be concluded from (23), (25), and (27) that I_g^*, I_K^*, and $Z_{N_{K-1}'}^{right}$ need not be considered for the calculation of $P(I_g)$, $P(I_K)$, and $P(Z_{N_{K-1}'}^{lr})$, respectively, due to the poles cancellation phenomena, as shown in (22), (24), and (26), respectively.

REFERENCES

[1] M. Liserre, R. Cardenas, M. Molinas, and J. Rodriguez, "Overview of multi-MW wind turbines and wind parks," IEEE Trans. Ind. Electron., vol. 58, no. 4, pp. 1081–1095, Apri. 2011.

[2] F. Blaabjerg, Z. Chen, and S. B. Kjaer, "Power electronics as efficient interface in dispersed power generation systems," IEEE Trans. Power Electron., vol. 19, no. 5, pp. 1184–1194, Sep. 2004.

[3] L. Harnefors, M. Bongiorno, and S. Lundberg, "Input-admittance calculation and shaping for controlled voltage-source converters," IEEE Trans. Ind. Electron., vol. 54, no. 6, pp. 3323–3334, Dec. 2007.

[4] X. Wang and F. Blaabjerg, "Harmonic stability in power electronic-based power systems: Concept, modeling, and analysis," IEEE Trans. Smart Grid, vol. 10, no. 3, pp. 2858–2870, May 2019.

[5] Y. Hu, S. Bu, B. Zhou, Y. Liu, and C.-W. Fei, "Impedance-based oscillatory stability analysis of high power electronics-penetrated power systems—a survey," IEEE Access, vol. 7, pp. 120 774–120 787, 2019.

[6] J. Segundo-Ramirez, A. Bayo-Salas, M. Esparza, J. Beerten, and P. Gómez, "Frequency domain methods for accuracy assessment of wide-band models in electromagnetic transient stability studies," IEEE Trans. Power Del., vol. 35, no. 1, pp. 71–83, Feb. 2020.

[7] L. Fan, "Modeling type-4 wind in weak grids," IEEE Trans. Sustain. Energy, vol. 10, no. 2, pp. 853–864, Apr. 2019.

[8] H. Liu and X. Xie, "Comparative studies on the impedance models of VSC-based renewable generators for SSI stability analysis," IEEE Trans. Energy Convers., vol. 34, no. 3, pp. 1442–1453, Sep. 2019.

[9] Y. Li, L. Fan, and Z. Miao, "Wind in weak grids: Low-frequency oscillations, subsynchronous oscillations, and torsional interactions," IEEE Trans. Power Syst., vol. 35, no. 1, pp. 109–118, Jan. 2020.

[10] W. Zhou, Y. Wang, R. E. Torres-Olguin, and Z. Chen, "Effect of reactive power characteristic of offshore wind power plant on low-frequency stability," IEEE Trans. Energy Convers., vol. 35, no. 2, pp. 837–853, Jun. 2020.

[11] L. Fan and Z. Miao, "A modular small-signal analysis framework for inverter penetrated power grids: Measurement, assembling, aggregation, and stability assessment," arXiv preprint arXiv:2003.03860, 2020.

[12] R. D. Middlebrook, "Input filter consideration in design and application of switching regulators," in Proc. IEEE IAS Annu. Meet., 1976, pp. 336–382.

[13] M. Belkhayat, "Stability criteria for AC power systems with regulated loads," Ph.D. dissertation, Purdue University West Lafayette, NI, 1997.

[14] J. Sun, "Impedance-based stability criterion for grid-connected inverters," IEEE Trans. Power Electron., vol. 26, no. 11, p. 3075, Nov. 2011.

[15] F. Liu, J. Liu, H. Zhang, and D. Xue, "Stability issues of Z+ Z type cascade system in hybrid energy storage system (HESS)," IEEE Trans. Power Electron., vol. 29, no. 11, pp. 5846–5859, Nov. 2014.

[16] W. Cao, Y. Ma, L. Yang, F. Wang, and L. M. Tolbert, "D–Q impedance based stability analysis and parameter design of three-phase inverter-based AC power systems," IEEE Trans. Ind. Electron., vol. 64, no. 7, pp. 6017–6028, Jul. 2017.

[17] C. Zhang, M. Molinas, A. Rygg, and X. Cai, "Impedance-based analysis of interconnected power electronics systems: Impedance network modeling and comparative studies of stability criteria," IEEE J. Emerg. Sel. Top. Power Electron., vol. 8, no. 3, pp. 2520–2533, Sep.. 2020.

[18] W. Zhou, R. E. Torres-Olguin, Y. Wang, and Z. Chen, "A gray-box hierarchical oscillatory instability source identification method of multiple-inverter-fed power systems," IEEE J. Emerg. Sel. Top. Power Electron., Early Access, doi: 10.1109/JESTPE.2020.2992225.

[19] W. Cao, Y. Ma, and F. Wang, "Sequence-impedance-based harmonic stability analysis and controller parameter design of three-phase inverter-based multibus ac power systems," IEEE Trans. Power Electron., vol. 32, no. 10, pp. 7674–7693, Oct. 2017.

[20] B. Gustavsen and A. Semlyen, "Rational approximation of frequency domain responses by vector fitting," IEEE Trans. Power Del., vol. 14, no. 3, pp. 1052–1061, Jul. 1999.

[21] B. Gustavsen, "Improving the pole relocating properties of vector fitting," IEEE Trans. Power Del., vol. 21, no. 3, pp. 1587–1592, Jul. 2006.

[22] M. K. Bakhshizadeh, C. Yoon, J. Hjerrild, C. L. Bak, Ł. H. Kocewiak, F. Blaabjerg, and B. Hesselbæk, "The application of vector fitting to eigenvalue-based harmonic stability analysis," IEEE J. Emerg. Sel. Top. Power Electron., vol. 5, no. 4, pp. 1487–1498, Dec. 2017.

[23] M. K. Bakhshizadeh, F. Blaabjerg, J. Hjerrild, Ł. Kocewiak, and C. L. Bak, "Improving the impedance based stability criterion by using the vector fitting method," IEEE Trans. Energ. Convers., vol. 33, no. 4, pp. 1739–1747, Dec. 2018.

[24] W. Zhou, Y. Wang, and Z. Chen, "A gray-box parameters identification method of voltage source converter using vector fitting algorithm," in Proc. IEEE 2019 10th International Conference on Power Electronics and ECCE Asia (ICPE 2019-ECCE Asia), pp. 2948–2955.

[25] W. Zhou, Y. Wang, P. Cai, and Z. Chen, "A gray-box impedance reshaping method of grid-connected inverter for resonance damping," in Proc. IEEE 2019 10th International Conference on Power Electronics and ECCE Asia (ICPE 2019-ECCE Asia), pp. 2660–2667.

[26] A. Rygg and M. Molinas, "Apparent impedance analysis: A small-signal method for stability analysis of power electronic-based systems," IEEE J. Emerg. Sel. Top. Power Electron., vol. 5, no. 4, pp. 1474–1486, Dec. 2017.

[27] H. Liu, X. Xie, and W. Liu, "An oscillatory stability criterion based on the unified *dq*-frame impedance network model for power systems with

This article has been accepted for publication in a future issue of this journal, but has not been fully edited. Content may change prior to final publication. Citation information: DOI 10.1109/OJIES.2020.3045620,
IEEE Open Journal of the Industrial Electronics Society

Zhou *et al.*: Electromagnetic Oscillation Origin Location

high-penetration renewables," IEEE Trans. Power Syst., vol. 33, no. 3, pp. 3472–3485, May 2018.

[28] H. Liu, X. Xie, X. Gao, H. Liu, and Y. Li, "Stability analysis of SSR in multiple wind farms connected to series-compensated systems using impedance network model," IEEE Trans. Power Syst., vol. 33, no. 3, pp. 3118–3128, May 2018.

[29] Y. Zhan, X. Xie, H. Liu, H. Liu, and Y. Li, "Frequency-domain modal analysis of the oscillatory stability of power systems with high-penetration renewables," IEEE Trans. Sustain. Energy, vol. 10, no. 3, pp. 1534–1543, Jul. 2019.

[30] E. Ebrahimzadeh, F. Blaabjerg, X. Wang, and C. L. Bak, "Bus participation factor analysis for harmonic instability in power electronics based power systems," IEEE Trans. Power Electron., vol. 33, no. 12, pp. 10 341–10 351, Dec. 2018.

[31] ——, "Reducing harmonic instability and resonance problems in PMSG-based wind farms," IEEE J. Emerg. Sel. Top. Power Electron., vol. 6, no. 1, pp. 73–83, Mar. 2018.

[32] L. Hong, W. Shu, J. Wang, and R. Mian, "Harmonic resonance investigation of a multi-inverter grid-connected system using resonance modal analysis," IEEE Trans. Power Del., vol. 34, no. 1, pp. 63–72, Feb. 2019.

[33] X. Wang, F. Blaabjerg, and W. Wu, "Modeling and analysis of harmonic stability in an AC power-electronics-based power system," IEEE Trans. Power Electron., vol. 29, no. 12, pp. 6421–6432, Dec. 2014.

[34] W. Cao, Y. Ma, F. Wang, L. M. Tolbert, and Y. Xue, "Low-frequency stability analysis of inverter-based islanded multiple-bus AC microgrids based on terminal characteristics," IEEE Trans. Smart Grid, vol. 11, no. 5, pp. 3662–3676, Sep. 2020.

[35] Y. Li, Z. Shuai, X. Liu, Y. Chen, Z. Li, Y. Hong, and Z. J. Shen, "Stability analysis and location optimization method for multi-converter power systems based on nodal admittance matrix," IEEE J. Emerg. Sel. Top. Power Electron., Early Access, doi:10.1109/JESTPE.2019.2954560.

[36] C. Yoon, H. Bai, X. Wang, C. L. Bak, and F. Blaabjerg, "Regional modeling approach for analyzing harmonic stability in radial power electronics based power system," in Proc. IEEE 6th International Symposium on Power Electronics for Distributed Generation Systems (PEDG), 2015, pp. 1–5.

[37] W. Zhou, Y. Wang, and Z. Chen, "Impedance-decoupled modeling method of multiport transmission network in inverter-fed power plant," IEEE Trans. Ind. Appl., vol. 56, no. 1, pp. 611–621, Jan./Feb. 2020.

[38] W. Cao, X. Zhang, Y. Ma, and F. Wang, "Stability criterion and controller parameter design of radial-line renewable systems with multiple inverters," in 2016 IEEE Applied Power Electronics Conference and Exposition (APEC). IEEE, 2016, pp. 2229–2236.

[39] W. Zhou, R. E. Torres-Olguin, Y. Wang, and Z. Chen, "DQ impedance-decoupled network model-based stability analysis of offshore wind power plant under weak grid conditions," IET Power Electron., Early Access, doi: 10.1049/iet-pel.2019.1575.

[40] M. Cheah-Mane, L. Sainz, J. Liang, N. Jenkins, and C. E. Ugalde-Loo, "Criterion for the electrical resonance stability of offshore wind power plants connected through HVDC links," IEEE Trans. Power Syst., vol. 32, no. 6, pp. 4579–4589, Nov. 2017.

[41] M. Amin and M. Molinas, "A gray-box method for stability and controller parameter estimation in HVDC-connected wind farms based on nonparametric impedance," IEEE Trans. Ind. Electron., vol. 66, no. 3, pp. 1872–1882, Mar. 2019.

[42] J. Huang, K. A. Corzine, and M. Belkhayat, "Small-signal impedance measurement of power-electronics-based AC power systems using line-to-line current injection," IEEE Trans. Power Electron., vol. 24, no. 2, pp. 445–455, Feb. 2009.

[43] A. Riccobono, M. Mirz, and A. Monti, "Noninvasive online parametric identification of three-phase AC power impedances to assess the stability of grid-tied power electronic inverters in LV networks," IEEE J. Emerg. Sel. Topics Power Electron., vol. 6, no. 2, pp. 629–647, Jun. 2018.

[44] T. Roinila, T. Messo, and E. Santi, "MIMO-identification techniques for rapid impedance-based stability assessment of three-phase systems in DQ domain," IEEE Trans. Power Electron., vol. 33, no. 5, pp. 4015–4022, May 2018.

[45] B. Wen, D. Boroyevich, R. Burgos, P. Mattavelli, and Z. Shen, "Inverse nyquist stability criterion for grid-tied inverters," IEEE Trans. Power Electron., vol. 32, no. 2, pp. 1548–1556, Feb. 2017.

[46] Y. Cho, K. Hur, Y. C. Kang, and E. Muljadi, "Impedance-based stability analysis in grid interconnection impact study owing to the increased adoption of converter-interfaced generators," Energies, vol. 10, no. 9, p. 1355, 2017.

[47] Z. Shuai, Y. Li, W. Wu, C. Tu, A. Luo, and Z. J. Shen, "Divided DQ small-signal model: A new perspective for the stability analysis of three-phase grid-tied inverters," IEEE Trans. Ind. Electron., vol. 66, no. 8, pp. 6493–6504, Aug. 2019.

[48] C. Zheng, Q. Li, L. Zhou, B. Li, and M. Mao, "The interaction stability analysis of a multi-inverter system containing different types of inverters," Energies, vol. 11, no. 9, p. 2244, 2018.

[49] W. Cao, S. Wang, H. Kang, K. Liu, Q. Wang, and J. Zhao, "Inherent interaction analysis for harmonic oscillations in the multi-paralleled grid-connected inverter system using a sum type criterion: Global admittance (GA)," IEEE Access, vol. 8, pp. 8275–8285, 2020.

[50] C. Zhang, X. Cai, M. Molinas, and A. Rygg, "On the impedance modeling and equivalence of AC/DC-side stability analysis of a grid-tied type-iv wind turbine system," IEEE Trans. Energy Convers., vol. 34, no. 2, pp. 1000–1009, Jun. 2019.

WEIHUA ZHOU (Student Member, IEEE) was born in Anhui, China, in 1993. He received the B.Eng. and M.Sc. degrees in electrical engineering from the School of Automation, Northwestern Polytechnical University, Xi'an, China, in 2014 and 2017, respectively. He is currently working toward the Ph.D. degree in electrical engineering with the Department of Energy Technology, Aalborg University, Aalborg, Denmark.

From November 2015 to May 2016, he was a Junior Research Assistant at the Department of Mechanical and Automation Engineering, the Chinese University of Hong Kong, Hong Kong. From August 2020 to November 2020, he was a visiting scholar at the Department of Marine Technology, Norwegian University of Science and Technology, Trondheim, Norway. His research interests include modeling and control of grid-connected converters, and small-signal stability analysis of power electronic-dominated power systems.

Mr. Zhou was the recipient of the Best Paper Award in 6th International Conference on Smart Grids (icSmartGrid) cosponsored by IEEE Industry Application Society in 2018.
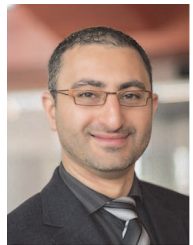
RAYMUNDO E. TORRES-OLGUIN received the B.Sc. degree in electromechanical engineering from the University of San Luis Potosí, Mexico, in 2004, M.Sc. degree in control and dynamical systems from the Applied Mathematics Department, Research Institute of Science and Technology of San Luis Potosí (IPICYT), Mexico, in 2006, and Ph.D. degree in electric power engineering from the Norwegian University of Science and Technology (NTNU), Norway, in 2013.

From 2012, he has worked as a research scientist in SINTEF Energy Research located in Trondheim, Norway. His main research interest includes control of power electronics for the integration of renewable resources, dc transmission, and microgrids.

MEHDI KARBALAYE ZADEH (Member, IEEE) received the Ph.D. degree in Electrical Engineering from NTNU, Trondheim, Norway, in 2016. From 2016 to 2017, he was with the power electronics industry, working on the development of battery charging systems. In 2017 he joined the Marine Technology Centre at NTNU in Trondheim, where he is currently an Associate Professor of Hybrid Power Systems and the director of the Marine Electrification Research Lab. His main research interests include ship electrification for low-emission and autonomous shipping, onboard DC power systems, and offshore renew-able energy systems.

YANBO WANG (Senior Member, IEEE) received the Ph.D. degree in electrical engineering at the Department of Energy Technology, Aalborg University, Aalborg, Denmark, in 2017. Currently, he is with the Department of Energy Technology in Aalborg University as an Assistant Professor.

From June to October of 2016, he was a visiting scholar in Power System Research Group of the Department of Electrical and Computer Engineering, University of Manitoba, Winnipeg, MB, Canada. His research interests include distributed power generation system, wind power system, microgrid, as well as operation and control technologies of power electronic-dominated power system.

Dr. Wang's paper on Distributed Power System received the First Prize Paper Award of the 6th International Conference of Smart Grid cosponsored by IEEE Industry Application Society in 2018. He received the Best Session Paper Award at the annual conference of the IEEE Industrial Electronics Society in 2015 in Japan.

BEHROOZ BAHRANI (Senior Member, IEEE) received the B.Sc. degree from Sharif University of Technology, Tehran, Iran, the M.Sc. degree from the University of Toronto, Toronto, ON, Canada, and the PhD degree from the Ecole Polytechnique Federale de Lausanne (EPFL), Lausanne, Switzerland, all in electrical engineering, in 2006, 2008, and 2012, respectively. From September 2012 to September 2015, he was a Postdoctoral Fellow at several institutions including EPFL, Purdue University, West Lafayette, IN, USA, Georgia Institute of Technology, At-lanta, GA, USA, and the Technical University of Munich, Munich, Germany. Currently, he is a Senior Lecturer at Monash University, where he is also serving as the Director of the Grid Innovation Hub. His research interests include control of power electronics systems, applications of power electronics in power and traction systems, and grid integration of renewable energy resources.

ZHE CHEN (Fellow, IEEE) received the B.Eng. and M.Sc. degrees all in electrical engineering from Northeast China Institute of Electric Power Engineering, Jilin City, China, MPhil in power electronic from Staffordshire University, England and the Ph.D. degree in electrical engineering from University of Durham, England.

Dr. Chen is a full Professor with the Department of Energy Technology, Aalborg University, Aalborg, Denmark. He is the leader of Wind Power System Research program at the Department of Energy Technology, Aalborg University and the Danish Principle Investigator for Wind Energy of Sino-Danish Centre for Education and Research. His research areas are power systems, power electronics and electric machines, and his main current research interests are wind energy and modern power systems. He has led many research projects and has more than 500 publications in his technical fields.